ORNL/TM-9869

ornl

OAK RIDGE NATIONAL LABORATORY

MARTIN MARIETTA

Electron Cyclotron Heating Calculations for ATF

R. C. Goldfinger
D. B. Batchelor

OPERATED BY
MARTIN MARIETTA ENERGY SYSTEMS, INC.
FOR THE UNITED STATES
DEPARTMENT OF ENERGY

Printed in the United States of America. Available from
National Technical Information Service
U.S. Department of Commerce
5285 Port Royal Road, Springfield, Virginia 22161
NTIS price codes—Printed Copy: A04; Microfiche A01

ORNL/TM-9869
Dist. Category UC-20 g

Fusion Energy Division

ELECTRON CYCLOTRON HEATING CALCULATIONS FOR ATF

R. C. GOLDFINGER
Computing and Telecommunications Division

D. B. BATCHELOR

Date Published - March 1986

Prepared by
OAK RIDGE NATIONAL LABORATORY
Oak Ridge, Tennessee 37831
operated by
MARTIN MARIETTA ENERGY SYSTEMS, INC.
for the
U.S. DEPARTMENT OF ENERGY
under Contract No. DE-AC05-84OR21400

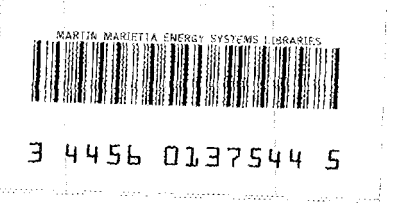

CONTENTS

ACKNOWLEDGMENTS

The authors thank J. H. Harris, T. L. White, and J. C. Glowienka for valuable discussions connected with this work. V. E. Lynch supplied the AVAC code and help with the plasma model.

ABSTRACT

The RAYS geometrical optics code has been used to calculate electron cyclotron wave propagation and heating in the Advanced Toroidal Facility (ATF) device under construction at Oak Ridge National Laboratory (ORNL). The intent of this work is to predict the outcome of various heating scenarios and to give guidance in designing an optimum heating system. Particular attention is paid to the effects of wave polarization and antenna location. We investigate first and second harmonic cyclotron heating with the parameters predicted for steady-state ATF operation. We also simulate the effect of wall reflections by calculating a uniform, isotropic flux of power radiating from the wall. These results, combined with the first-pass calculations, give a qualitative picture of the heat deposition profiles. From these results we identify the compromises that represent the optimum heating strategies for the ATF model considered here. Our basic conclusions are that second harmonic heating with the extraordinary mode (X-mode) gives the best result, with fundamental ordinary mode (O-mode) heating being slightly less efficient. Assuming the antenna location is restricted to the low magnetic field side, the antenna should be placed at $\phi = 0°$ (the toroidal angle where the helical coils are at the sides) for fundamental heating and at $\phi = 15°$ (where the helical coils are at the top and bottom) for second harmonic heating. These recommendations come directly from the ray tracing results as well as from a theoretical identification of the relevant factors affecting the heating.

1. INTRODUCTION

This paper presents results for electron cyclotron heating using a 53.2-GHz microwave source in the plasma regime that should provide a target plasma for neutral beam injection [T_e = 500 eV, $n_e \sim 10^{13}$ cm^{-3}, $|\overline{B}_0| \sim 1.9$ T and 0.95 T (first and second harmonic, respectively)]. The main objective of the study is to determine how to maximize the first-pass absorption of the beam and how to have this heating occur as near as possible to the magnetic axis. When the magnetic field level is adjusted to place the cyclotron resonance at the axis ($f_{ce} = eB/2\pi MC = 53.2$ GHz and $2f_{ce} = 53.2$ GHz on axis for the first and second harmonic absorption, respectively) the absorption will occur near the axis, but it may not be total. The damping strength is a function of the plasma parameters for the desired polarization and of the local scale length in $|\overline{B}|$. Thus the optimum power deposition profile will be a compromise between maximizing the absorption and having the heating occur near the axis. Other considerations in choosing the optimum launch configuration result from sensitivity of the results to antenna characteristics and plasma parameters. For example, finite beta effects and small changes in vertical field currents can radially displace the magnetic axis location. These factors can help point to a preferred launch position.

Our calculations are based on one assumed set of coil currents that gives rise to a nominal ATF configuration with the magnetic axis located at 210 cm. The rotational transform profile is $\iota(0) = 0.33$ and $\iota(a) = 1.0$, where $a = 30$ cm is the plasma radius. Since other current configurations significantly change the topology of the magnetic field and the flux surfaces, the recommendations we make concerning optimum launching are valid only for this particular configuration. However, the same general principles and analysis can be applied to other field configurations, which can be readily analyzed with our code. The complicated topology of the mod-B resonance surfaces and their relationship to the location of the magnetic axis are shown to be the primary factors in determining the wave absorption. Specifically, the maximum absorption occurs when the resonance occurs at the saddle point of the magnetic field. Other considerations, such as natural symmetries in the system, the separation between the saddle point and the magnetic axis, and the gradient perpendicular to the ray trajectories, all help to point to a preferred launch location for any given equilibrium.

The ray tracing is done using cold plasma theory to propagate the rays according to the results of geometrical optics [1,2]. We treat each case by doing two runs: a single-pass calculation of the incident beam and a calculation that simulates the effect of the remaining power. This remaining power is treated by assuming that the part of the beam not absorbed on the first pass is quickly randomized in direction, location, and polarization

throughout the device. We base the model on our experience with the ELMO Bumpy Torus (EBT) experiment. Hence, we can estimate the effect of the initial beam plus subsequent wall reflections by a superposition of the two cases. We present results for both high- and low-field launch, although only low-field operation is planned on ATF at this time. It will be shown that the O-mode polarization ($\vec{E} \parallel \vec{B}$ for perpendicular propagation) is strongly absorbed at the fundamental cyclotron resonance. The X-mode cannot reach the fundamental resonance from the low-field side because of the presence of the right-hand cutoff. When the magnetic field level is decreased to the point at which the plasma center is resonant at the second harmonic of the wave frequency, the roles of the O- and X-modes are reversed. For this case, the X-mode can reach the second harmonic [as long as $f_{pe}(0) < (53.2\ \mathrm{GHz})/\sqrt{2}$] and is very strongly absorbed. The O-mode is weakly absorbed at the second harmonic and makes an insignificant contribution to second harmonic heating.

The organization of the paper is as follows. Section 2 presents some of the theoretical background of the RAYS code. Specifically discussed are cold plasma ray tracing, the finite temperature approximations used in calculating the damping, and details about the plasma model. Section 3 displays the ray tracing calculations, and Section 4 presents the conclusions.

2. THEORETICAL BACKGROUND

2.1. THE RAYS CODE

RAYS, a code first developed at ORNL for the study of electron cyclotron heating in EBT [1–3], traces rays in an arbitrary magnetized plasma configuration. The ray tracing is carried out by integrating the Hamiltonian form of the geometrical optics equations using the two-component, cold plasma dispersion relation:

$$\frac{d\bar{r}}{ds} = \frac{1}{|\bar{V}_g|}\frac{d\bar{r}}{dt} = -\mathrm{sgn}\left(\frac{\partial D}{\partial \omega}\right)\frac{\partial D/\partial \bar{k}}{|\partial D/\partial \bar{k}|} \tag{1}$$

and

$$\frac{d\bar{k}}{ds} = \frac{1}{|\bar{V}_g|}\frac{d\bar{k}}{dt} = \mathrm{sgn}\left(\frac{\partial D}{\partial \omega}\right)\frac{\partial D/\partial \bar{r}}{|\partial D/\partial \bar{k}|} \tag{2}$$

where

$$\begin{aligned}
D &= \left[\left(\varepsilon_1 - n_\parallel^2\right)\left(\varepsilon_1 - n^2\right) - \varepsilon_2^2\right]\left(\varepsilon_3 - n_\perp^2\right) \\
&\quad - \left[n_\parallel^2 n_\perp^2\left(\varepsilon_1 - n^2\right)\right] = 0 \\
\varepsilon_1 &= 1 - \frac{\omega_{pe}^2}{\omega^2 - \omega_{ce}^2} - \frac{\omega_{pi}^2}{\omega^2 - \omega_{ci}^2} \\
\varepsilon_2 &= -\frac{\omega_{pe}^2}{\omega}\frac{\omega_{ce}}{\omega^2 - \omega_{ce}^2} - \frac{\omega_{pi}^2}{\omega}\frac{\omega_{ci}}{\omega^2 - \omega_{ci}^2} \\
\varepsilon_3 &= 1 - \frac{\omega_{pe}^2}{\omega^2} - \frac{\omega_{pi}^2}{\omega^2} \\
\omega_{pe,i} &= \left(\frac{4\pi n_e^2}{m_{e,i}}\right)^{\frac{1}{2}} \\
\omega_{ce,i} &= \frac{eB}{m_{e,i}}
\end{aligned} \tag{3}$$

Here, $\bar{n} = c\bar{k}/\omega$ is the real refractive index, $n_\parallel = \bar{n}\cdot\hat{B}$, and $n_\perp = \sqrt{n^2 - n_\parallel^2}$. For the case of weak absorption considered here the effect of finite temperature on the ray trajectories can be neglected [4]. We can develop insight into this dispersion relation for the regime of interest if we consider a simplified form that comes from assuming that $\omega \sim \omega_{ce} >> \omega_{ci}$ and $n \sim n_\perp >> n_\parallel$. Under these approximations, Eq. (3) becomes

$$\begin{aligned}
&\left(1 - \frac{\omega_{pe}^2}{\omega^2} - \frac{\omega_{ce}^2}{\omega^2}\right)n_\perp^4 - \left[\left(1 - \frac{\omega_{pe}^2}{\omega^2}\right)\left(1 - \frac{\omega_{pe}^2}{\omega^2} - \frac{\omega_{ce}^2}{\omega^2}\right)\right. \\
&\left. + \left(1 - \frac{\omega_{pe}^2}{\omega^2}\right) - \frac{\omega_{ce}^2}{\omega^2}\right]n_\perp^2 + \left(1 - \frac{\omega_{pe}^2}{\omega^2}\right)\left[\left(1 - \frac{\omega_{pe}^2}{\omega^2}\right)^2 - \frac{\omega_{ce}^2}{\omega^2}\right] = 0
\end{aligned} \tag{4}$$

The two roots of this biquadratic equation in $n_\perp^2$ correspond to the O- and X-polarization modes. A resonance occurs in the X-mode (the upper hybrid resonance) when the coefficient of the $n_\perp^4$ term vanishes: $1 - \omega_{pe}^2/\omega^2 - \omega_{ce}^2/\omega^2 = 0$. Cutoffs occur in both branches when the constant term vanishes:

$$1 - \frac{\omega_{pe}^2}{\omega^2} = 0 \qquad \text{(O-mode cutoff)}$$

$$\left(1 - \frac{\omega_{pe}^2}{\omega^2}\right)^2 - \frac{\omega_{ce}^2}{\omega^2} = 0 \qquad \text{(X-mode cutoff)}$$

For the 53.2-GHz wave source, the O-mode will be unable to penetrate the plasma center when the density exceeds $n_e = 3.5 \times 10^{13}$ cm^{-3}. An X-mode ray from the low magnetic field side will encounter the right-hand cutoff and be reflected before the ray can reach the fundamental cyclotron resonance surface, $\omega_{ce}/\omega = 1$ (except for a small fraction of X-mode power that can tunnel through the evanescent region on the outer edge of the plasma). The question of whether the X-mode can reach the second harmonic before hitting the cutoff when launched from the low-field side depends on the density: when $\omega_{pe}^2/\omega^2 < 0.5$ (which corresponds to a density of 1.75×10^{13} cm^{-3} for 53.2 GHz), the ray can reach the second harmonic.

For high-field launch the situation is as follows. An O-mode ray incident from the high-field side will be able to reach the fundamental resonance as long as the density is below O-mode cutoff, $n_e = 3.5 \times 10^{13}$ cm^{-3}. A high-field X-mode ray will first encounter the fundamental resonance, $\omega_{ce}/\omega = 1$, and then possibly the upper hybrid layer, $\omega_{pe}^2/\omega^2 + \omega_{ce}^2/\omega^2 = 1$. There is very weak absorption of the X-mode at the fundamental resonance for $n_\perp >> n_\parallel$, but strong absorption near the upper hybrid resonance by mode conversion to electron Bernstein modes [5–7]. If oblique propagation is done, $n_\parallel \sim n_\perp$, then very strong high-field X-mode absorption occurs near the fundamental resonance. The density cutoff for this case is $\omega_{pe}^2/\omega^2 = 2$ or $n_e = 7 \times 10^{13}$ cm^{-3}. Due to the difficulty of high-field oblique launching, no such experiments are planned, and hence no calculations are done in this paper for high-field X-mode launch. As is shown below, it turns out that the X-mode is much more strongly absorbed at the second harmonic than the O-mode. Thus, in summary, the best strategy for low-field launch is to use X-mode polarization when the central magnetic field makes the second harmonic resonant there ($|\overline{B}_0| \sim 0.95$ T). When the field is increased to cause the fundamental resonance to appear near the center ($|\overline{B}_0| \sim 1.9$ T), then accessibility requires O-mode launch.

2.2. WAVE ABSORPTION

The fractional absorption of wave energy due to cyclotron damping is given by

$$f(s) = 1 - \exp\left(-2\int_0^s \bar{k}_i \cdot d\bar{s}\right) \tag{6}$$

where k_i is the imaginary part of the wave vector and s is the path length along the ray. In order to perform the integration in Eq. (6), it is necessary to determine $\bar{k}_i \cdot d\bar{s}$ as a function of s. The value of $\bar{k}_i$ that corresponds to damping at the fundamental cyclotron resonance is obtained from a weak damping approximation for oblique propagation similar to that given in Ref. [8]. In this application, we expand about the local value of $(n_\parallel, n_\perp)$ as given by the RAYS code. The component of $\bar{k}_i$ in the direction of $\bar{k}$ is given by

$$k_i = \frac{\omega}{c} \cdot \mathrm{Im}\left[-\frac{D^{\mathrm{w}}\left(\mathbf{n}^0\right)}{\hat{\mathbf{n}}^0 \cdot \frac{\partial D^C}{\partial n^0}}\right] = \frac{\omega}{c} \cdot \mathrm{Im}\left[-\frac{D^{\mathrm{w}}\left(\mathbf{n}^0\right)}{\frac{n_\perp^0}{|\mathbf{n}^0|}\frac{\partial D^C}{\partial n_\perp^0} + \frac{n_\parallel^0}{|\mathbf{n}^0|}\frac{\partial D^C}{\partial n_\parallel^0}}\right] \tag{7}$$

Here D^C is the cold plasma dispersion relation, $n_\parallel^0$ and $n_\perp^0$ are the zero-order refractive indices obtained directly from the integration of the ray equations, and D^W is a warm plasma correction term of the form

$$D^W = -\frac{\omega + |\Omega_e|}{\omega} n_\parallel \frac{v_e}{c}\left(D_1 + D_2 + \frac{n_\perp^2}{2n_\parallel}\frac{\omega^2}{\Omega_e^2}\frac{v_e}{c}\varsigma\right)\left[\varsigma + \frac{1}{Z(\varsigma)}\right] \tag{8}$$

where

$$D_1 = (1-q)\,n^2 n_\perp^2 + (1-P)\,n^2 n_\parallel^2 - (1-q)\,(1-P)\left(n^2 + n_\parallel^2\right) - (1-2q)\,n_\perp^2 + (1-2q)\,(1-P)$$

$$D_2 = P\frac{\omega}{|\Omega_e|}\left[n^2 n_\perp^2 - (1-2q)\,n_\perp^2\right] + P^2\frac{\omega}{4\Omega_e^2}\left[\frac{n_\perp^2}{n_\parallel^2}\left(n^2 + n_\parallel^2\right) - 2\,(1-2q)\,\frac{n_\perp^2}{n_\parallel^2}\right]$$

$$D_3 = P\left[n^2 n_\parallel^2 - (1-q)\left(n^2 + n_\parallel^2\right) + (1-2q)\right]$$

$$P = \frac{\omega_{pe}^2}{\omega^2} \quad q = \frac{\omega_{pe}^2}{2\omega\,(\omega + |\Omega_e|)} \quad \varsigma = \frac{\omega - |\Omega_e|}{k_\parallel v_e} \quad v_e = \left(\frac{2T_e}{m_e}\right)^{\frac{1}{2}}$$

and $Z(\varsigma)$ is the plasma dispersion function.

For nearly perpendicular propagation, $n_\parallel \lesssim v/c$, relativistic effects predominate. In this regime our code approximates $n_\parallel = 0$ and uses the Shkarofsky formulation [9] to numerically solve

$$n_\perp^2 - (\varepsilon_3 + \varepsilon_{zz}^{\mathrm{w}}) = 0\,, \quad \text{O-mode}$$

$$n_\perp^2 (\varepsilon_1 + \varepsilon_{xx}^{\mathrm{w}}) - (\varepsilon_1 + \varepsilon_{xx}^{\mathrm{w}})(\varepsilon_1 + \varepsilon_{yy}^{\mathrm{w}}) - (\varepsilon_2 + \varepsilon_{xy}^{\mathrm{w}})^2 = 0\,, \quad \text{X-mode}$$

where

$$\begin{aligned}
\varepsilon_{xx}^{\mathrm{w}} &= \frac{-\mu}{2}\frac{\omega_{pe}^2}{\omega^2}\left(F_{\frac{5}{2}} - \lambda F_{\frac{7}{2}} + \frac{5}{8}\lambda^2 F_{\frac{9}{2}}\right) \\
\varepsilon_{xy}^{\mathrm{w}} &= -i\frac{\mu}{2}\frac{\omega_{pe}^2}{\omega^2}\left(F_{\frac{5}{2}} - 2\lambda F_{\frac{7}{2}} + \frac{15}{8}\lambda^2 F_{\frac{9}{2}}\right) \\
\varepsilon_{yy}^{\mathrm{w}} &= -\frac{\mu}{2}\frac{\omega_{pe}^2}{\omega^2}\left(F_{\frac{5}{2}} - 3\lambda F_{\frac{7}{2}} + \frac{37}{8}\lambda^2 F_{\frac{9}{2}}\right) \\
\varepsilon_{zz}^{\mathrm{w}} &= -\frac{\mu}{2}\frac{\omega_{pe}^2}{\omega^2}\lambda\left(F_{\frac{7}{2}} - \lambda F_{\frac{9}{2}}\frac{7}{12}\lambda^2 F_{\frac{11}{2}}\right) \\
F_q(\zeta) &= F_q\left(\mu\frac{\omega - 2|\Omega_e|}{\omega}\right) = -i\int_0^\infty \frac{dt}{1 - it}e^{i\zeta t} \\
\mu &= \frac{c}{v_e^2} \\
\lambda &= k_\perp^2 v_e^2/\Omega_e^2
\end{aligned} \tag{9}$$

Using these approximations, Fig. 1 shows the O-mode k_i as a function of magnetic field strength (normalized to the wave frequency) around the fundamental resonance for various values of $n_\parallel$. It is seen that as the wave vector becomes more nearly perpendicular to the magnetic field (small values of $n_\parallel$), the damping is confined to an increasingly narrow region in space on the high-field side of the resonance.

The X-mode damping near the second harmonic is obtained using Poynting's theorem,

$$\frac{d|\overline{S}|}{ds} = \frac{4\pi}{c}\overline{E}^* \cdot \overline{\overline{\sigma}}^H \cdot \overline{E} \tag{10}$$

where $\overline{S} = \mathrm{Re}\left[\overline{E}^* \times (\overline{n} \times \overline{E})\right]$ is the Poynting's vector and $\overline{\overline{\sigma}}^H$ is the Hermitian part of the relativistic conductivity tensor. The model for $\overline{\overline{\sigma}}^H$ assumes an isotropic Maxwellian distribution and allows contributions from an arbitrary number of cyclotron harmonics. (For this application, only the $n = 2$ term contributes.) The real refractive index is determined from the ray tracing code; the electric field eigenvectors, $\overline{E}$, used in the absorption equation are determined from the cold plasma dispersion tensor, $\overline{D} \cdot \overline{E} = 0$. Details on the calculations for $\overline{\overline{\sigma}}^H$ may be found in Ref. [10]. Figure 2 shows k_i as a function of magnetic field around the second harmonic. A comparison of Figs. 1 and 2 reveals that the X-mode absorption at the second harmonic is between two and five times greater than the O-mode absorption at the fundamental, with the line shapes quite similar for the two cases.

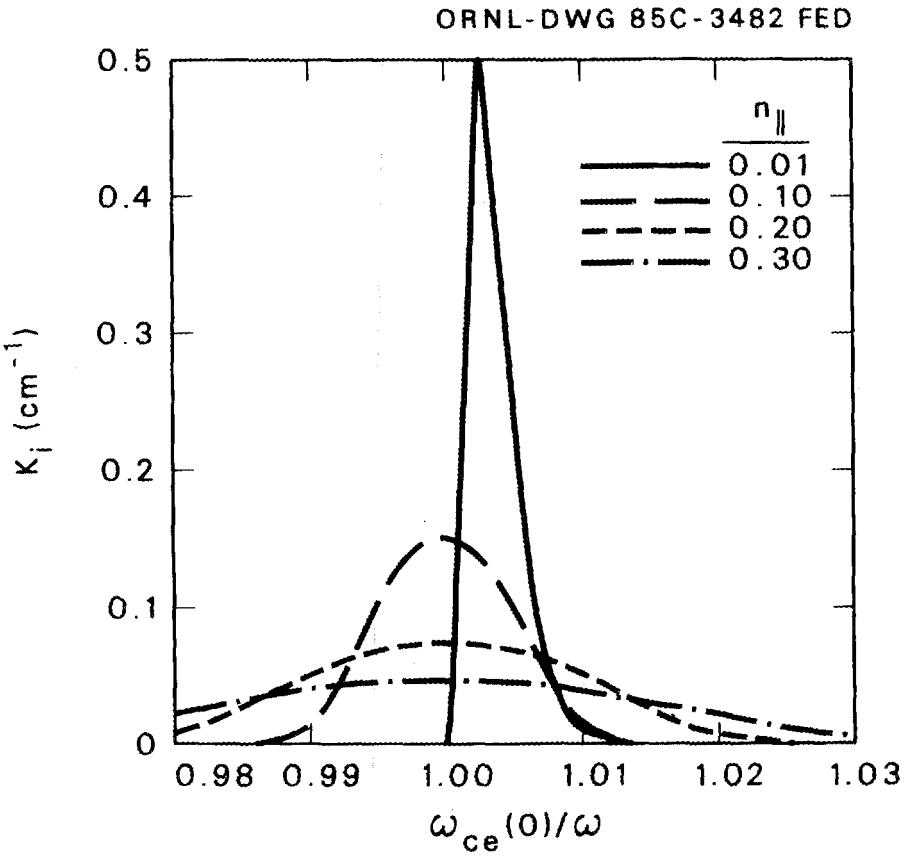

FIG. 1. The imaginary part of the O-mode wave vector, k_i, as a function of normalized magnetic field strength, ω_{ce}/ω.

2.3. PLASMA MODEL

For the magnetic field model we have used the three-dimensional vacuum field code, AVAC [11–13], developed by V. E. Lynch and others. AVAC uses the Biot-Savart law to calculate the magnetic field that results from an arbitrary configuration of external currents. Its considerable generality and flexibility allow the accurate calculation of vacuum fields in torsatrons, stellarators, helical-axis devices, and other machines. It is shown here that magnetic topology is the significant factor in determining the power deposition profile as well as the total absorption. This sensitivity implies that it is essential to use an accurate, fully three-dimensional magnetic field for these calculations to get meaningful results.

We approximate the magnetic field in ATF by using AVAC with two filamentary helical field (HF) coils and four vertical field (VF) coils in a configuration appropriate for ATF. The

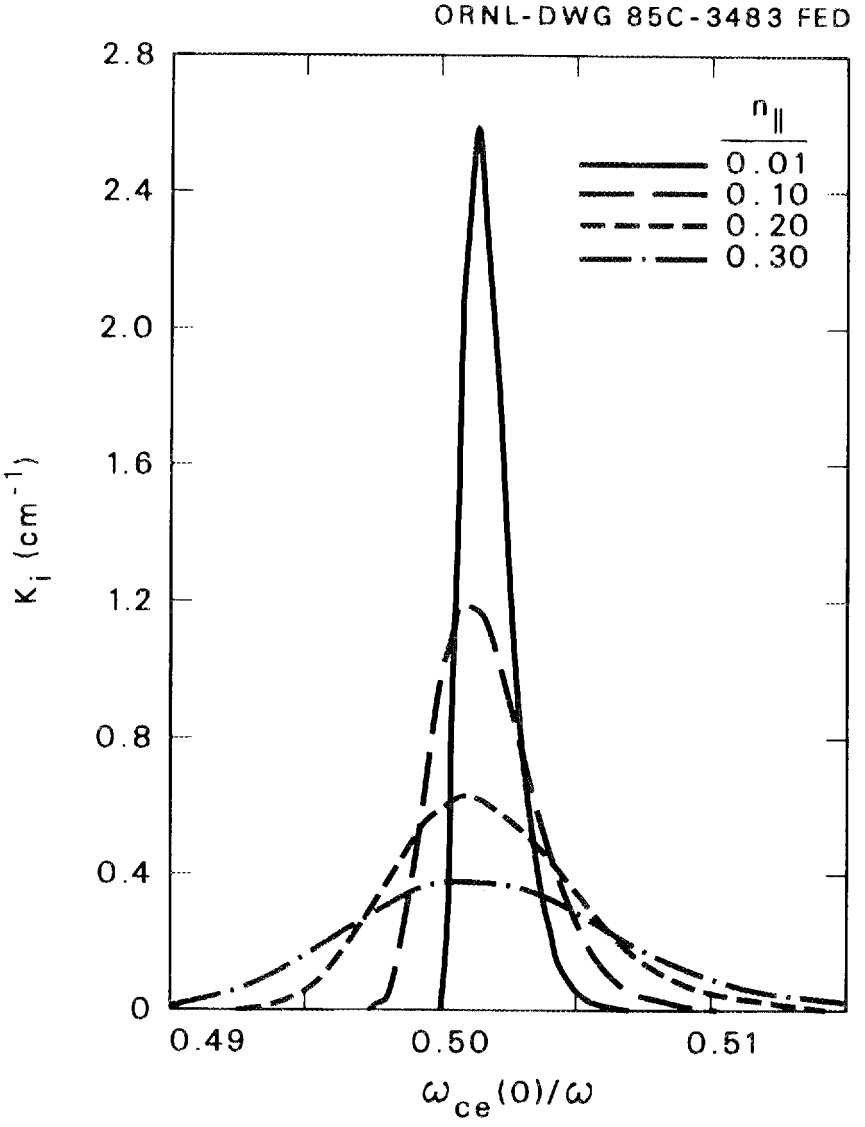

FIG. 2. The imaginary part of the X-mode wave vector, k_i, as a function of normalized magnetic field strength, ω_{ce}/ω.

two HF coils carry equal current with major radius of 210.0 cm and minor radius of 48.0 cm. The VF coils are located at R (cm), Z (cm) = (281.0, 61.7), (281.0, −61.7), (133.0, 20.0) and (133.0, −20.0). The outer VF coils carry 47% of the HF coil current anti-parallel to the direction of the HF current, while the inner VF coils carry 15% of the HF current in the same sense. Ampère's law applied to the HF coils shows that a current of 0.875 MA produces a magnetic field on axis (R = 210.0 cm) of $|B_0|$ = 1.0 T. The plasma density and electron temperature are assumed constant on a flux surface and therefore are parameterized by the toroidal magnetic flux function, ψ. The dependence of density and electron temperature on minor radius, $n_e(\psi)$, is illustrated in Fig. 3. For the toroidal flux function we have used an ad hoc "rotating ellipse" model that is a reasonable representation (at least for the purposes of ray tracing) of the vacuum flux function. In this model, the flux surfaces are elliptical in a plane of constant toroidal angle, ϕ, and rotate about the minor axis with the helical windings. These ellipses are concentric and centered at $R = R_{MAJOR}$ = 210 cm.

In Fig. 4 we show (a) the resonance and (b) the cutoff surfaces described in Section 2.1. We have plotted the electron cyclotron resonance, the upper hybrid resonance, and the right-hand cutoff for $|B_0|$ = 1.9 T and $n_e = 10^{13}$ cm^{-3}. Because an O-mode ray experiences no resonances or cutoffs for this density, the entire chamber is accessible to it. An X-mode ray is evanescent in the region between the right-hand cutoff and cyclotron resonance so that it cannot reach the plasma center when launched from the low-field side with these parameters. When an X-mode ray is launched from the high-field side, it reaches the cyclotron resonance but does not encounter the upper hybrid resonance unless it is propagating at considerably oblique angles. This leads us to conclude that mode conversion and absorption near the upper hybrid resonance play an insignificant role for these parameters.

Figures 5–7 show mod-B and flux contours on various surfaces for ATF. Each figure has three contours of constant flux, indicated by dotted lines that correspond to plasma densities (or temperatures) in our model of 90%, 50%, and 20% of the maximum value at the magnetic axis, $\psi = 0$. The solid lines are contours of constant $|\overline{B}|$ that are labeled according to the normalized value of $|\overline{B}|$ on each contour. The contour with value 1.0 passes through the magnetic axis, $\psi = 0$, in the $\phi = 0°$ plane. Thus, for a wave frequency of 53.2 GHz, this surface is the location of the cyclotron resonance if $|\overline{B}|$ = 1.9 T at this point, $(x, y, z) = (210, 0, 0)$. Figures 5 and 6 are poloidal cross sections in the toroidal planes $\phi = 0°$ and $\phi = 15°$, respectively. In the $\phi = 0°$ plane the helical windings are at the sides of the vacuum chamber, while at $\phi = 15°$ the windings are at the top and bottom of the chamber. Figure 7 displays the contours on the orthogonal surface, $R = \sqrt{(x^2 + y^2)} = 210$ cm. (This is the cylindrical sheet containing the minor axis.) We

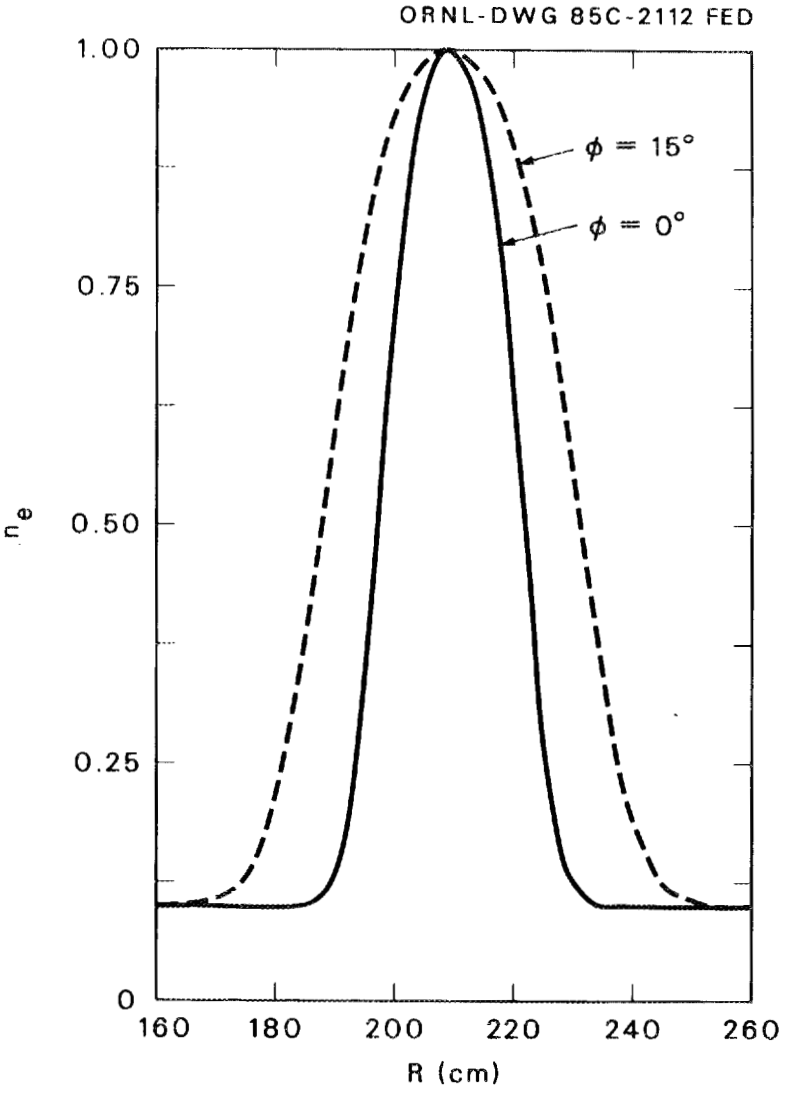

FIG. 3. Normalized electron density, or temperature, as a function of major radius for $\phi = 0°$ and $\phi = 15°$. The maximum density occurs on the minor axis, $R = 210$ cm; the asymptotic density is 10% of the maximum.

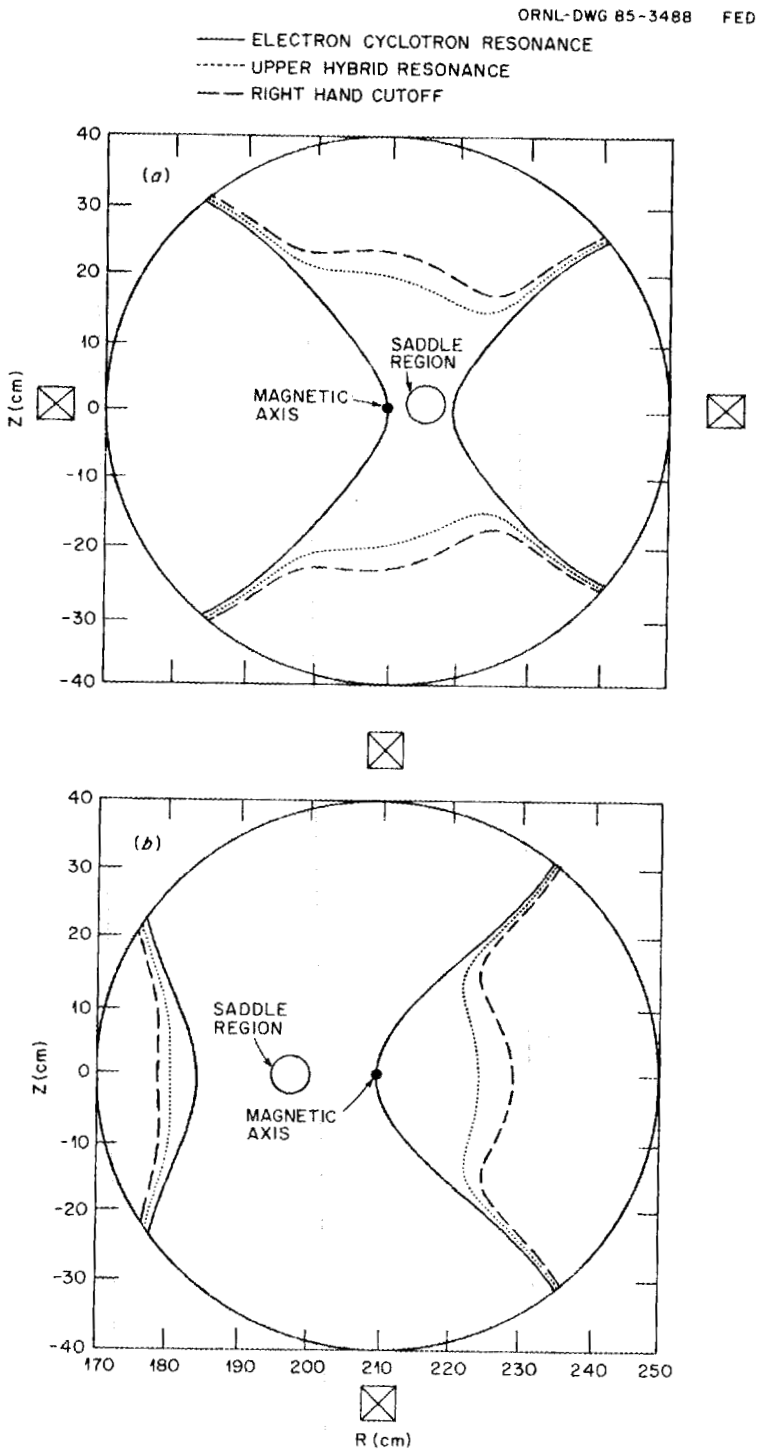

FIG. 4. The fundamental electron cyclotron resonance, upper hybrid resonance, and right-hand cutoff surfaces for $|\overline{B}_0| = 1.9$ T, $n_e = 1.0 \times 10^{13}$ cm^{-3}. The intersections of these surfaces with (a) the $\phi = 0°$ and (b) the $\phi = 15°$ toroidal planes are shown.

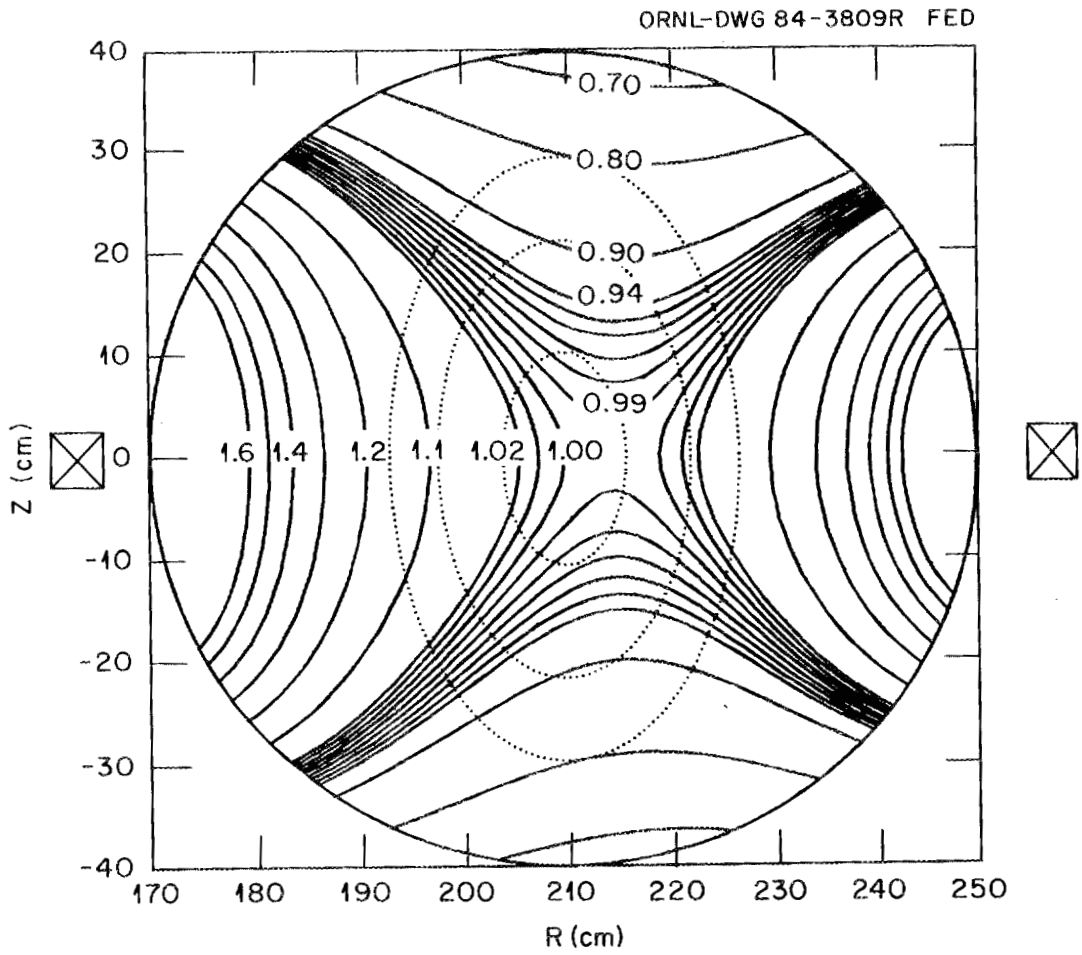

FIG. 5. Mod-B and flux contours in the $\phi = 0°$ plane. The ellipses represent contours of 90%, 50%, and 20% density. The value of $|\overline{B}|$ on each contour is indicated, normalized to unity on the magnetic axis, $R = 210$ cm. The helical windings are at $R = 210 \pm 48$ cm, $Z = 0$ in this plane.

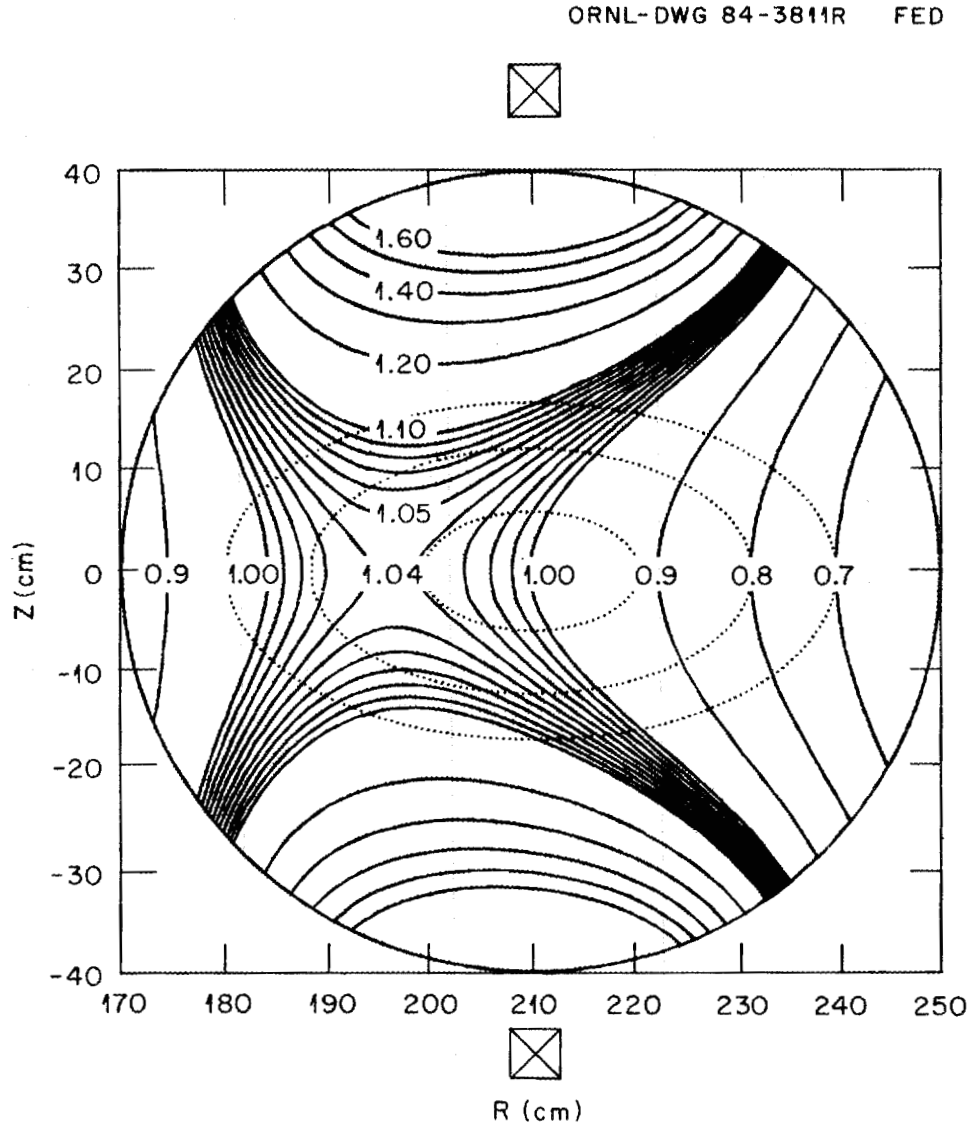

FIG. 6. Mod-B and flux contours in the $\phi = 15°$ plane. The helical windings are at the top and bottom of the torus in this plane.

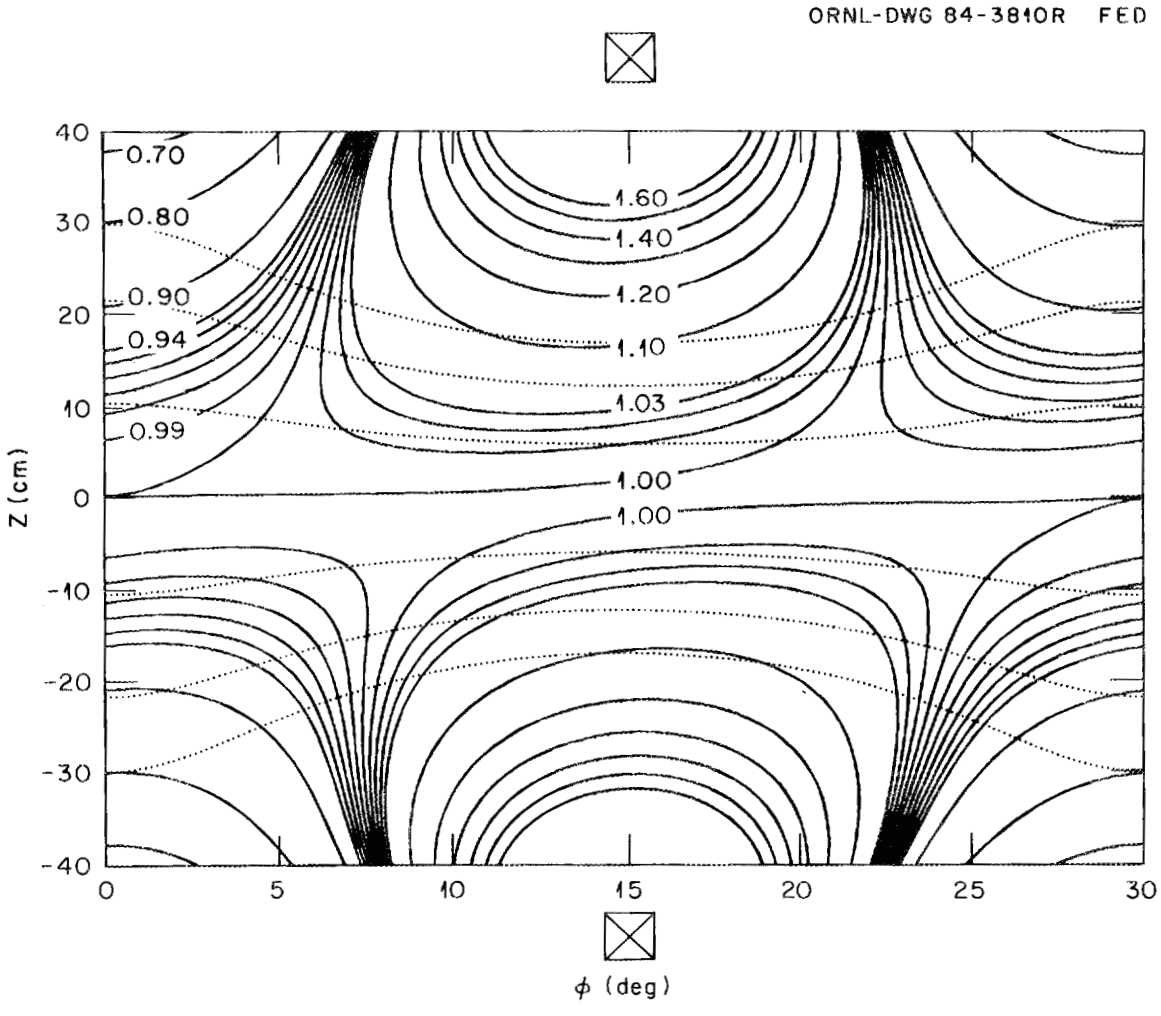

FIG. 7. Mod-B and flux contours on the cylindrical surface, $R = 210$ cm. The helical windings are at the top and bottom for $\phi = 15°$ in this plane. The magnetic axis lies in the plane of the page at $Z = 0$.

can make a number of predictions about wave absorption, which are borne out by the ray tracing calculations, by inspecting these figures. First, a surface with an arbitrary value of $|\overline{B}|$ is generally quite complicated in this torsatron geometry. Inspection of the poloidal cuts, Figs. 5 and 6, shows a saddle point in the field near the center and a strong variation of $\nabla|\overline{B}|$ across the plasma. Because the damping is strongly localized in space in regions around $\omega_{ce}(\overline{r}) = \omega$, it is clear that the damping will be much greater when the resonance is near the saddle point than when it lies on an off-center mod-B contour. Thus, for maximum first-pass absorption, it is crucial to choose the gyrotron frequency such that the magnetic field level can be adjusted to make this saddle point region resonant.

A comparison of Figs. 5 and 6 illustrates the importance of toroidal effects; the two figures differ in several significant ways beyond the simple poloidal rotation of the helical coils. Because the value of $|B|$ at the saddle point is approximately 5% higher at $\phi = 15°$ than it is at $\phi = 0°$, the plane of launching will affect the values of optimum magnetic field level and/or gyrotron frequency. Another toroidal effect not seen in a straight (cylindrical) model is that the branches of mod-B are not symmetric with respect to the magnetic axis; thus, inside launch from the midplane will be different from outside launch, for example. A more subtle effect is the difference in topology between the two planes. Note that both of these planes have up/down symmetry in the magnetic field. This means that low-field launch from $\phi = 15°$ (along a horizontal line in the midplane) is in a symmetry plane, whereas low-field launch from $\phi = 0°$ (from the top or bottom) is not. Therefore, with low-field $\phi = 15°$ launch, the beam is assured of passing through both the magnetic axis and the saddle point when the boresight is directed toward the minor axis. This is not the case with $\phi = 0°$ launch; here the beam (which is nearly vertical), the magnetic axis, and the saddle point are not colinear in general. Finite beta, varying VF coil currents, and other effects will move these points out of the fixed beam path. Thus, aiming of the beam will be more difficult and sensitive to operating conditions for low-field $\phi = 0°$ launch. Since the saddle point and axis lie on the midplane, another consequence of the up/down symmetry is that when the axis is made resonant, the resonant contour will be a "no-miss" contour when the beam is launched from the midplane. That is, the resonant contour that passes through the axis encloses the beam for $\phi = 15°$ low-field launch, but it does not enclose the beam for $\phi = 0°$ low-field launch (see Fig. 4). Consequently, a portion of the beam will miss the resonance for the $\phi = 0°$ top launch case. In summary, then, launching from the midplane along a horizontal line (low-field $\phi = 15°$ or high-field $\phi = 0°$) has some theoretical advantages. The finite spread of the beam in the complicated magnetic geometry moderates this conclusion somewhat, but the basic effects described here are borne out by the ray tracing calculations.

3. RAY TRACING CALCULATIONS

3.1. INTRODUCTION

Numerous calculations are presented in this section for various launch positions and magnetic fields. With fixed launch point, density, and temperature, the magnetic field strength is changed, making various mod-B contours resonant. We plot the absorption as a function of field strength and show power deposition profiles for selected points on the curve. This heating profile is a histogram in ψ space (ψ = toroidal flux), $dP(\psi)/d\psi$, in which ψ has been mapped into two different radial coordinates. These radial coordinates, R_{HIGH} and R_{LOW}, correspond to the given value of $\psi(r)$ as one moves away from the magnetic axis in the high- and low-field directions, respectively. The histogram is thus an approximation of the heat deposited per unit volume at the given radius.

Two types of calculations are presented: first-pass runs and wall reflection runs. The first-pass runs simulate the effect of the beam on its first pass through the plasma. These calculations take a conical bundle of eight rays, emanating from a point, to simulate a beam with a full width at half maximum of approximately 3°. This is done by launching eight rays with azimuthal angles of $\theta_{RAY} = 0.5°$, 1.5° and polar angles of $\phi_{RAY} = 0°$, 90°, 180°, 270° about the chosen beam direction. The wall reflection runs give an indication of where the power not absorbed on the first pass is deposited in the plasma. There are several mechanisms by which this residual power can be left after the first pass through the plasma. The most obvious ways are a mixture of polarization modes at the center and plasma parameters that cause a given wave to experience less than 100% absorption. Less than 100% first-pass absorption can also occur due to beam collimation and aiming errors or to magnetic field structure different from that modeled in this idealized picture (e.g., finite beta effects). From this wall reflection calculation we determine how much of the randomized power is absorbed per bounce, and we obtain a heating profile for where this power is deposited.

Section 3 is organized as follows. Initially we discuss the first-pass calculations, starting with the fundamental resonance. In Sections 3.2 and 3.3 we compare the results of launching from the high- and low-field sides for the $\phi = 0°$ and $\phi = 15°$ toroidal planes. Section 3.4 is a similar discussion for the second harmonic. The density chosen for these runs is 1.0×10^{13} cm^{-3}, which corresponds to $\omega_{pe}(0)/\omega = 0.53$. For each of these first-pass cases, we also include calculations done at higher densities approaching cutoff for the respective modes. For the fundamental resonance O-mode runs, the higher density used is 2.8×10^{13} cm^{-3}, which corresponds to $\omega_{pe}(0)/\omega = 0.9$ [O-mode cutoff is $\omega_{pe}(0)/\omega = 1.0$]. The high-density

second harmonic X-mode run (Section 3.5) was done with $n_e = 1.7 \times 10^{13}$ cm^{-3}, $\omega_{pe}(0)/\omega = 0.7$ [the right-hand cutoff eclipses the second harmonic resonance for $\omega_{pe}(0)/\omega = 1/\sqrt{2}$]. In Section 3.6 we briefly describe additional first-pass calculations that test some of the qualitative statements that have been made about magnetic symmetry and topology. In this section we test the sensitivity to beam width and the effect of a displaced magnetic axis. Finally, we discuss the wall reflection calculations and their impact on the heating process in Section 3.7.

3.2. LOW-FIELD LAUNCH, FUNDAMENTAL RESONANCE, FIRST-PASS CALCULATIONS

Figures 8–13 are first-pass calculations at the fundamental and second harmonic at $n_e = 1.0 \times 10^{13}$ cm^{-3}. As described in Section 2.1, the O-mode is strongly absorbed at the fundamental. In contrast, the X-mode beam does not intercept the upper hybrid resonance and is weakly absorbed for nearly perpendicular propagation at the cyclotron resonance. Thus, the first-pass fundamental resonance calculations are all done with the O-mode. Figures 8–13 compare low-field launch in the $\phi = 0°$ and $\phi = 15°$ toroidal planes. This corresponds to launching the beam from the top of the torus at $\phi = 0°$ (the helical coils are on the midplane) and from the outside of the midplane at $\phi = 15°$ (the helical coils are at the top and bottom). The ordinate of the graph in Figs. 10 and 12 is the power absorbed from the beam. The abscissa is the cyclotron gyrofrequency, evaluated at the magnetic axis and normalized to the wave frequency. Thus $\omega_{ce}(0)/\omega = 0.5$ and 1.0 correspond respectively to the second harmonic and fundamental resonance falling on the magnetic axis. The actual ray trajectories in space are shown in Figs. 8 and 9 for the points labeled "A" in Figs. 10 and 12. The ray trajectories for the other points (not shown) are similar. We immediately notice several features. First, inspection of Figs. 10 and 12 reveals that it is possible for 100% of the incident beam to be absorbed on the first pass when the field is such that the resonance falls near the saddle point and scale lengths are at their maximum. Since the magnetic axis and saddle point are not coincident, this means that the goal of maximum beam absorption may be in conflict with trying to deposit all the power near the axis. Figures 11 and 13 show the radial heating profiles for several selected points from Figs. 10 and 12. In Fig. 11b (point "F"), there is a net absorption of 96% when the field level is adjusted to make $\omega_{ce}(0)/\omega = 1.005$ for $\phi = 0°$ launch. This heating occurs close to the axis; all of the power is deposited within 5 cm of the axis in the high-field direction and 8 cm in the low-field direction. The situation for fundamental heating in the $\phi = 15°$ plane is not quite as good. In Fig. 13b (point "E") 98% absorption is achieved, but it occurs 10 cm from the axis in the low-field direction. If the field is now

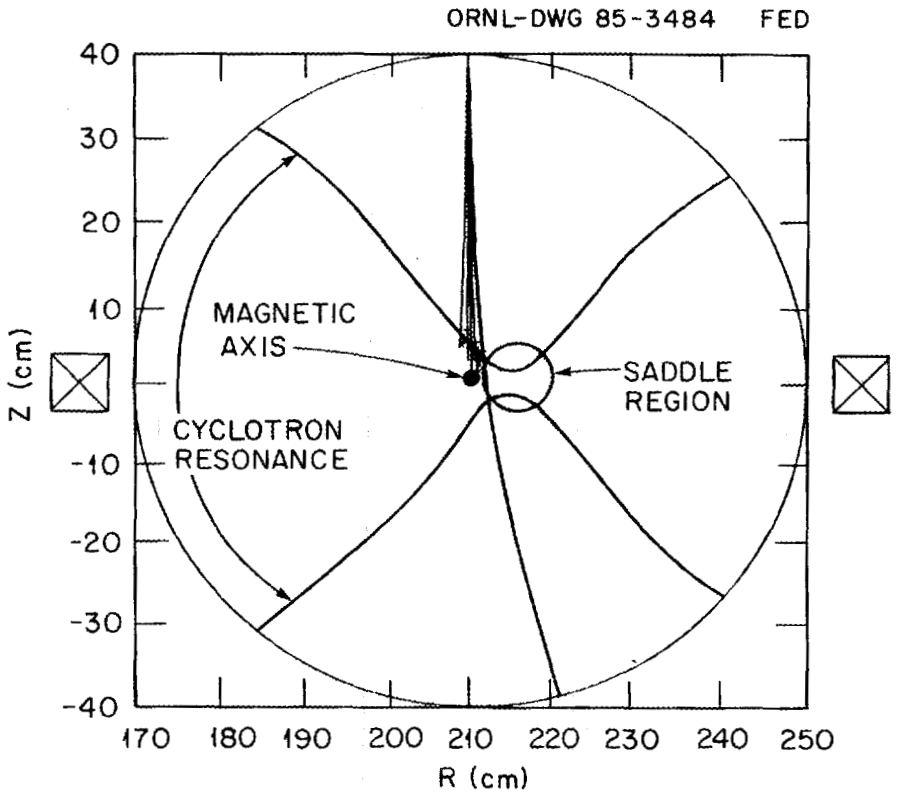

FIG. 8. Poloidal projection of X-mode rays launched from the top of the torus in the $\phi = 0°$ plane (low-field launch). The value of $|\overline{B}|$ at the magnetic axis, $(R, Z, \phi) = (210, 0, 0)$, is 0.95 T (second harmonic operation), and the asterisks indicate the approximate location of absorption. When 99% of the power of a ray is absorbed, the calculation is stopped for that ray. Some rays experience weak absorption because their trajectories (which may lie out of the plane of the paper) do not pass through the high-field side of the resonance (see Fig. 2).

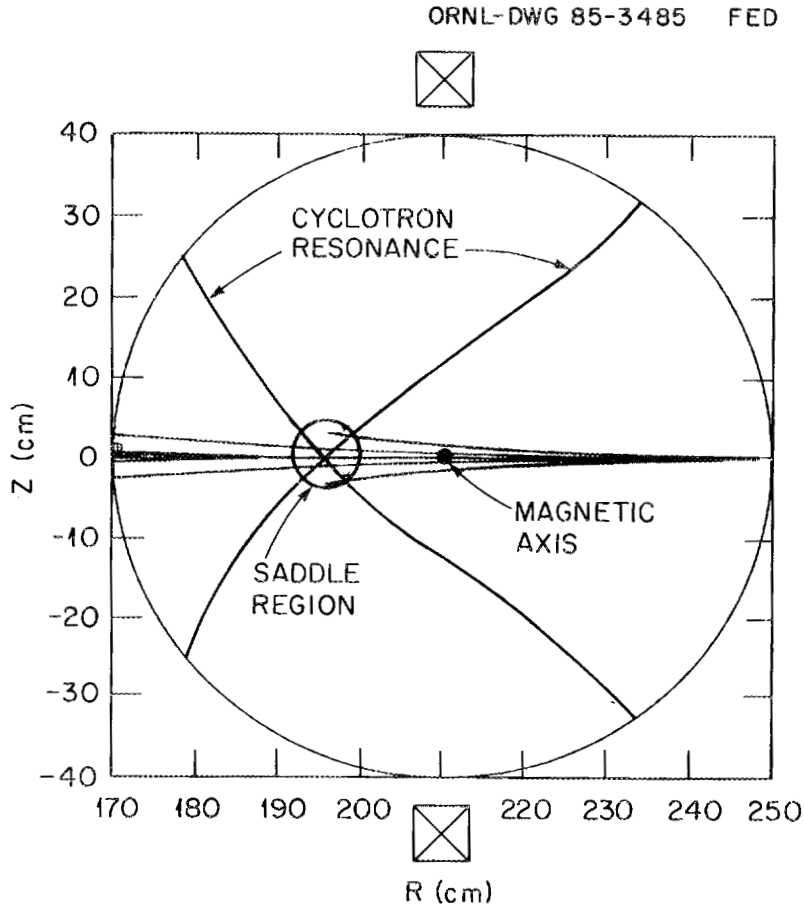

FIG. 9. Poloidal projection of X-mode rays launched from the midplane in the $\phi = 15°$ plane (low-field launch). The resonance lies on the saddle point. Rays that pass through the middle of the saddle region do not pass through the high-field side of the resonance and are therefore weakly absorbed.

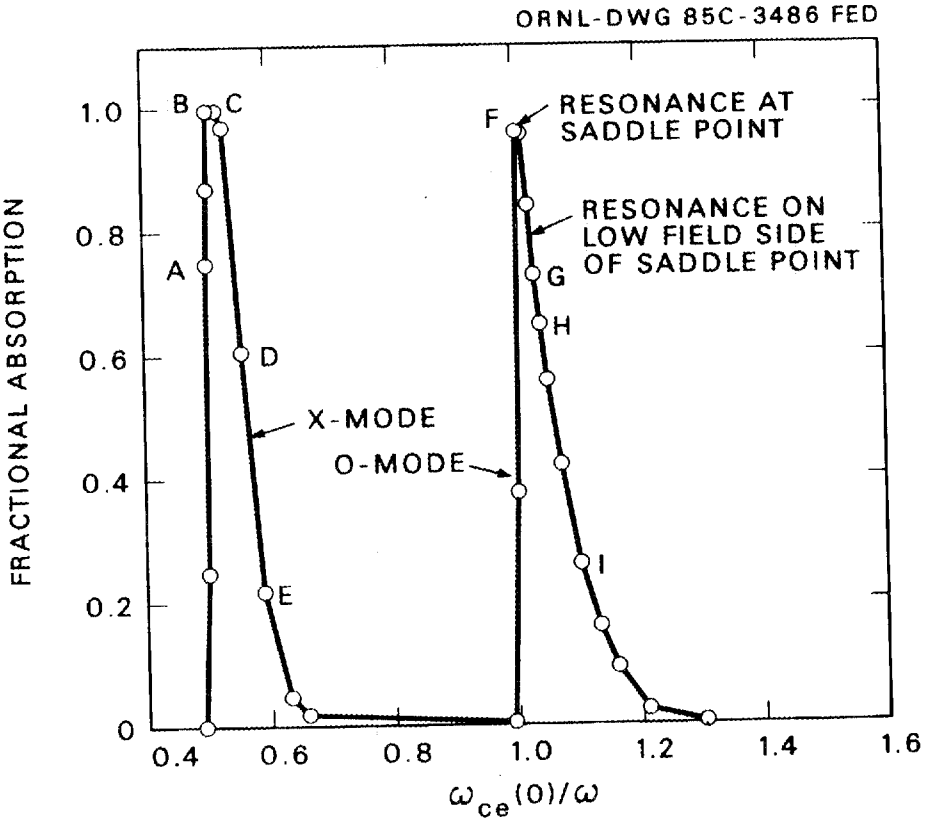

FIG. 10. Fractional absorption as a function of $\omega_{ce}(0)/\omega$ for top launch in the $\phi = 0°$ plane with $n_e = 10^{13}$ cm^{-3}.

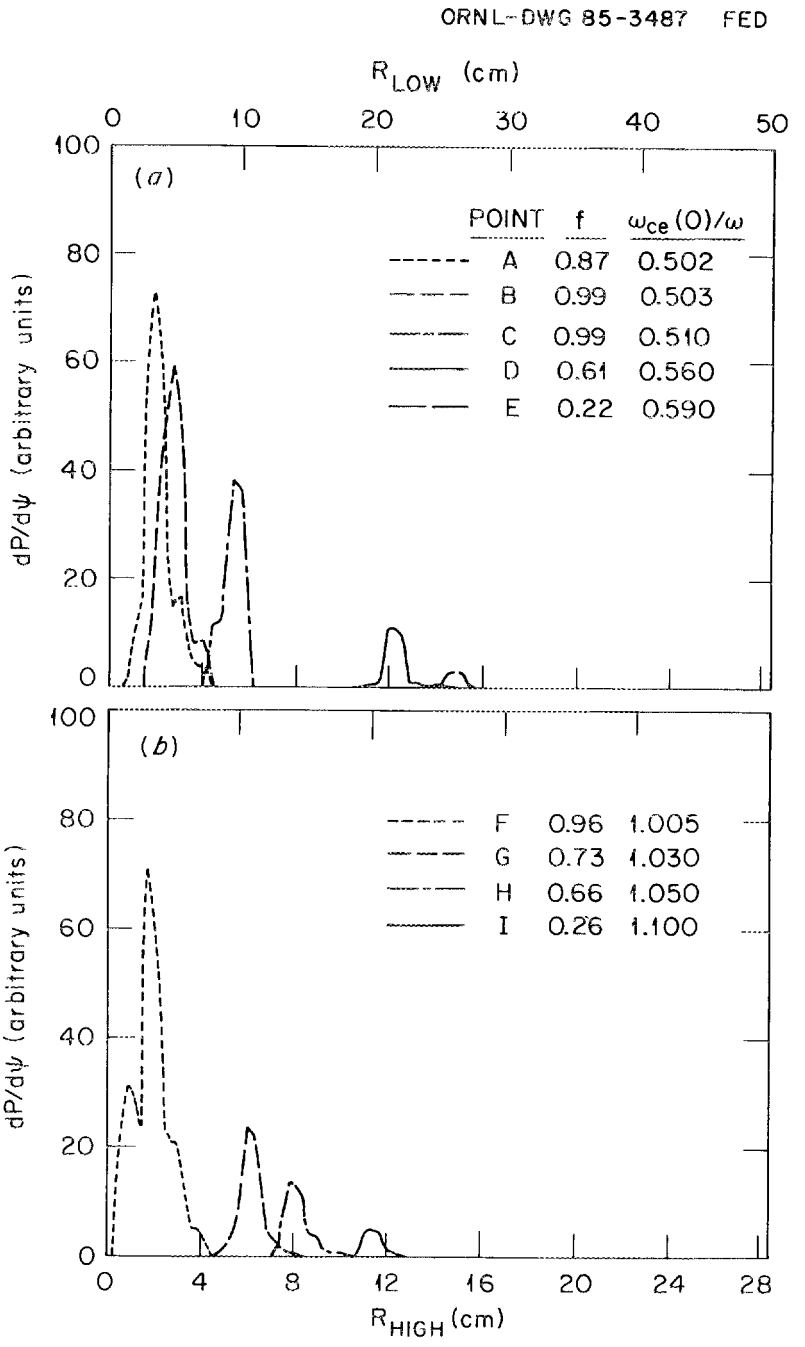

FIG. 11. Relative damping, $dP(\psi)/d\psi$ for selected points from Fig. 10. (a) Points for second harmonic operation; (b) points for fundamental operation. The damping rate at a given value of ψ is plotted against the two axes, R_{HIGH} and R_{LOW} (the R_{LOW} axis is on the top of the figure). R_{HIGH} (R_{LOW}) are the distances from the magnetic axis to the corresponding ψ value in the radial direction towards (away from) the helical coils.

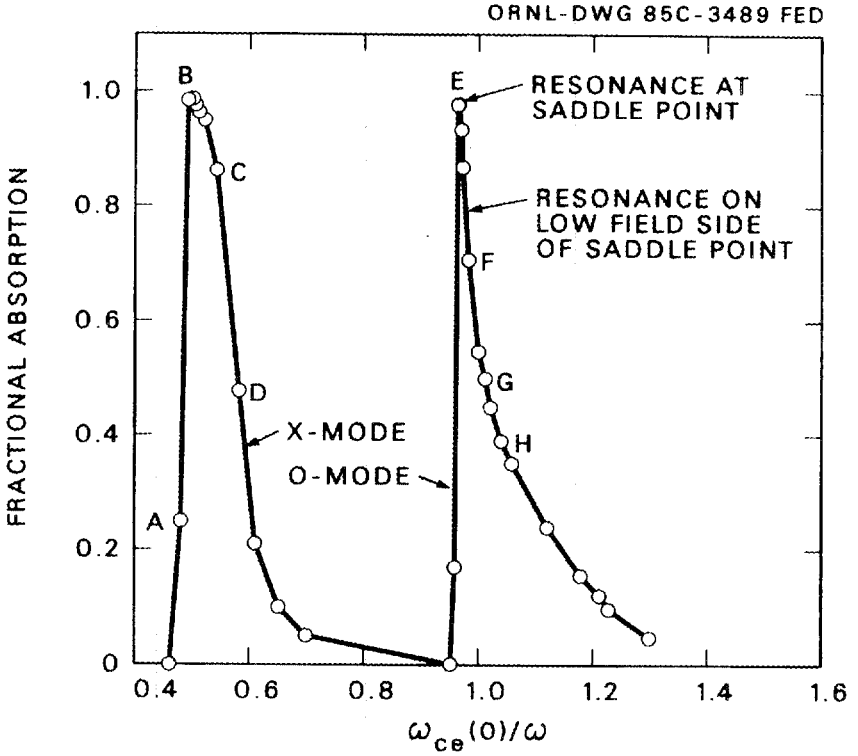

FIG. 12. Fractional absorption as a function of $\omega_{ce}(0)/\omega$ for midplane launch in the $\phi = 15°$ plane (low-field launch) with $n_e = 1.0 \times 10^{13}$ cm^{-3} [launch point $(R, \phi, Z) = (250, 15, 0)$].

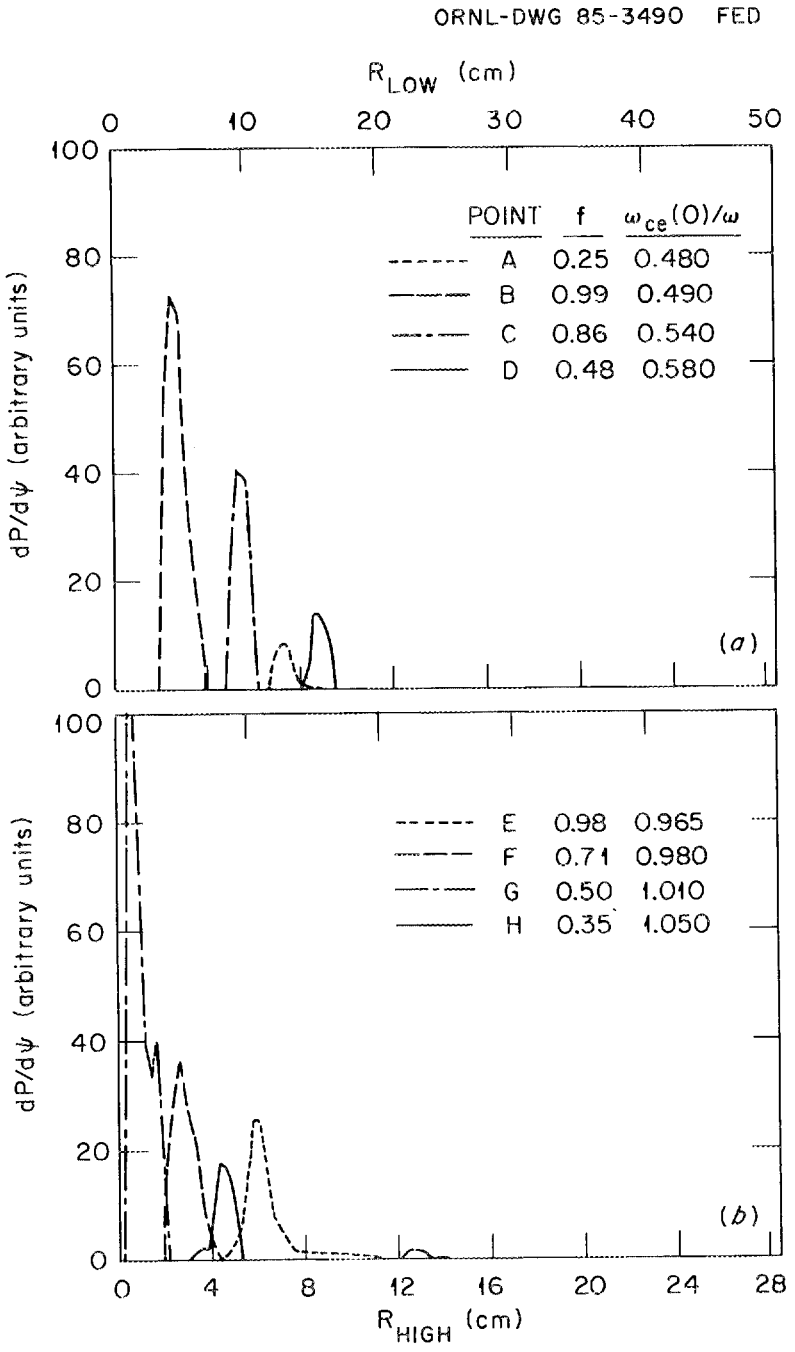

FIG. 13. Relative damping, $dP(\psi)/d\psi$, for selected points from Fig. 12.

adjusted to make the axis resonant in Fig. 13b (point "G"), the absorption falls to 50%. The reason for the difference between $\phi = 0°$ and $\phi = 15°$ is apparent from consulting Fig. 4. This figure shows that the magnetic axes and saddle points are closer at $\phi = 0°$ than they are at $\phi = 15°$. Thus, when the damping process is comparatively weak, as is the case here for the fundamental O-mode, the damping will only be strong when the resonance falls near the saddle point. It may be necessary to exploit the enhanced absorption that occurs at the saddle point when doing fundamental O-mode heating or when the density and temperature are lower (at startup, for example).

3.3. HIGH-FIELD LAUNCH, FUNDAMENTAL RESONANCE, FIRST-PASS CALCULATIONS

Figures 14–17 show the results of high-field launch in the $\phi = 0°$ plane with the O-mode. As with low-field launch, it is possible to get 100% absorption when the region near the saddle point is resonant. The striking difference between these figures and the previous ones is that the asymmetric, sawtooth-shaped absorption curves are mirror images of each other for low- and high-field launch. This is easily understood by an inspection of the mod-B contour plots, Figs. 5–7. Consider, for example, the low-field launch case discussed previously. Assume that the waves are launched from the midplane in the $\phi = 15°$ plane and that the resonance falls on the saddle point (see Fig. 6). As the field is increased, the resonant contour changes from the one labeled "1.04" to ones with lower numerical labels. Thus, the resonant contours encircle the launch point and move towards it, yielding a continuous, monotonically decreasing absorption (because of profile effects and the decreasing scale length for the field). If the field is decreased, however, the contours labeled 1.05, 1.06, etc., become resonant and first-pass absorption vanishes, since these contours lie out of the beam path. For high-field launch, the situation is reversed, with a continuous gradual decrease of power on the low-field side of the resonances. Including the effects of wall reflections (Section 3.7), which are not nearly as sensitive to field strength as the first-pass calculations, substantially reduces the asymmetry of the profile.

It is interesting to see the effect of toroidicity by comparing the difference between launching from the outside, Figs. 14 and 15, and inside, Figs. 16 and 17, of the midplane at $\phi = 0°$. Figure 4a shows that the difference between these two cases is that with inside launch the beam first passes through the resonance and axis simultaneously when the axis is made resonant. With outside launch, the beam encounters the other half of the resonance before it hits the resonant axis. Outside launch will, therefore, cause greater off-axis absorption. This is not seen in a straight torsatron model where the two branches of mod-B contours are symmetric with respect to the magnetic axis. Comparison of point

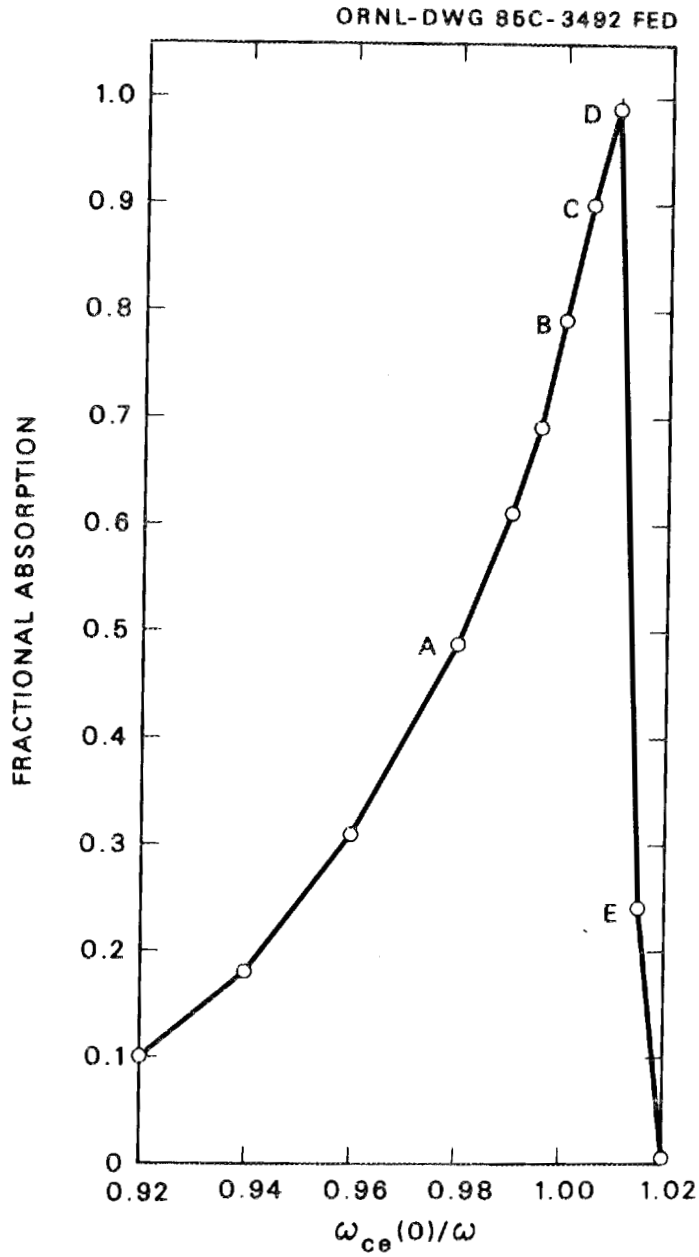

FIG. 14. Fractional absorption as a function of $\omega_{ce}(0)/\omega$ for high-field launch in the $\phi = 0°$ plane with $n_e = 10^{13}$ cm^{-3} [launch point, $(R, \phi, Z) = (250, 0, 0)$].

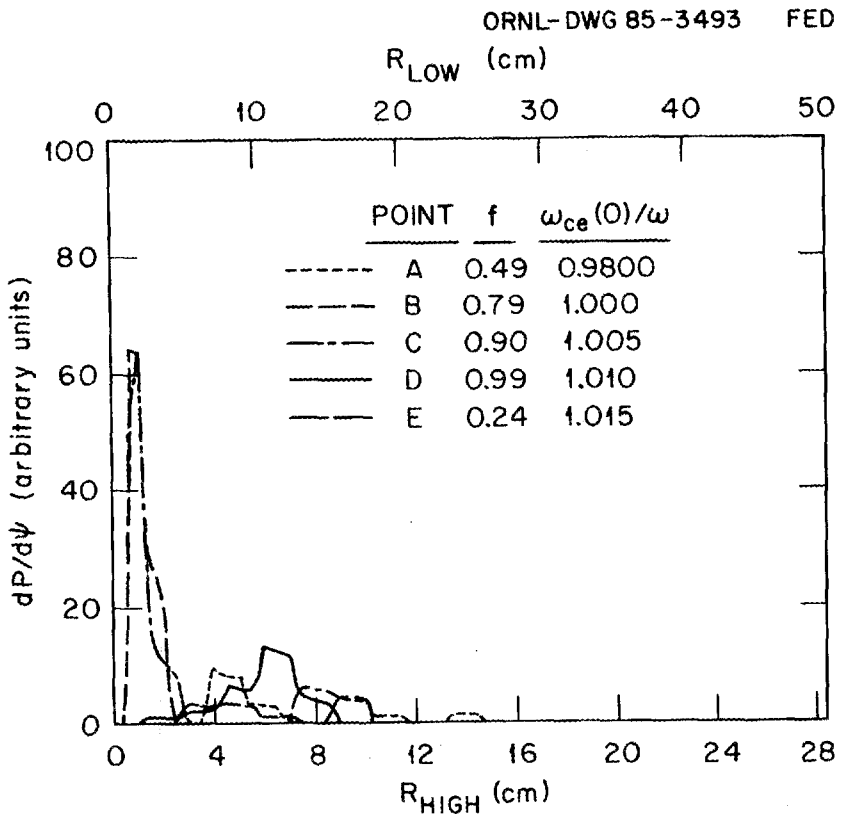

FIG. 15. Relative damping for selected points from Fig. 14.

"D" in Figs. 15 and 17 shows that with inside launch, 99% absorption can be obtained close to the axis. With outside launch and the same field level, 99% absorption results, but it occurs 10 cm farther out. Therefore, the optimal position for midplane launch is on the side from which the axis is encountered before the saddle point. This reasoning leads to the conclusion that midplane launch in the $\phi = 15°$ plane (low-field launch) is better from the outside than the inside (Fig. 4b).

3.4. LOW-FIELD LAUNCH, SECOND HARMONIC RESONANCE, FIRST-PASS CALCULATIONS

The second harmonic results are qualitatively similar to the fundamental results. Figures 1 and 2 show that the principal difference between fundamental and second harmonic absorption is that the second harmonic absorption is about two to five times as strong.

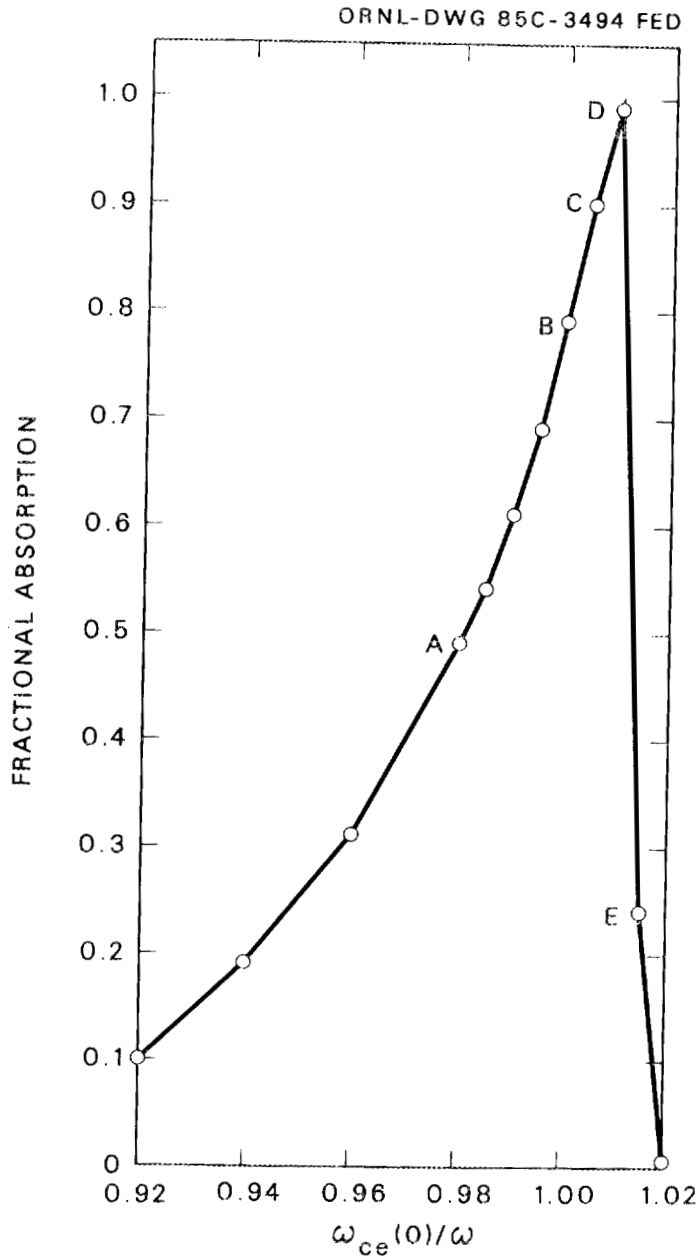

FIG. 16. Fractional absorption as a function of $\omega_{ce}(0)/\omega$ for high-field launch in the $\phi = 0°$ plane with $n_e = 10^{13}$ cm^{-3} [launch point, $(R, \phi, Z) = (170, 0, 0)$].

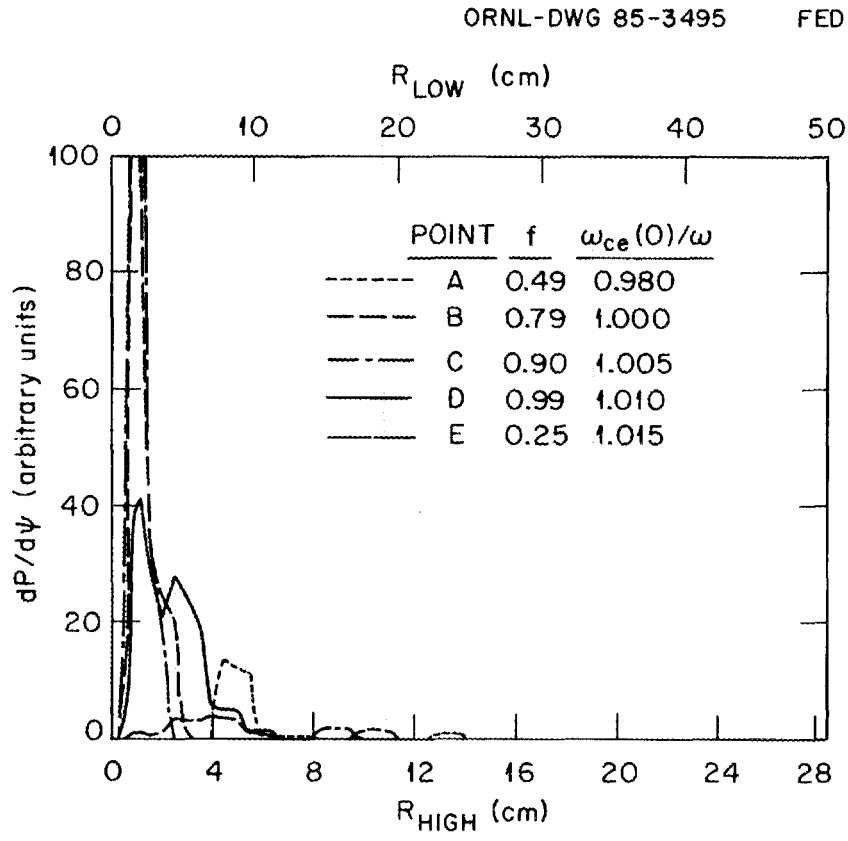

FIG. 17. Relative damping for selected points from Fig. 16.

This results in the fact that 100% second harmonic absorption can be achieved near the axis for both $\phi = 0°$ and $\phi = 15°$ launch (see point "B" in Figs. 11a and 13a). Recall that the scale length near the axis at $\phi = 15°$ is not large enough to permit strong, central damping at the fundamental resonance. The higher damping rate at the second harmonic, however, leads us to conclude that good results can be obtained for either launch plane at this density and temperature.

3.5. FIRST-PASS, HIGH-DENSITY CALCULATIONS

In order to see the effect of ray refraction due to high density, first-pass runs were done with the magnetic field adjusted to give optimum central absorption. This refraction is potentially a concern, particularly for top launch where the in/out asymmetry exaggerates the deflection of rays away from the center. The density was chosen slightly below cutoff for the O- and X-modes in Figs. 18–21. Figures 18 and 19 show O-mode rays launched

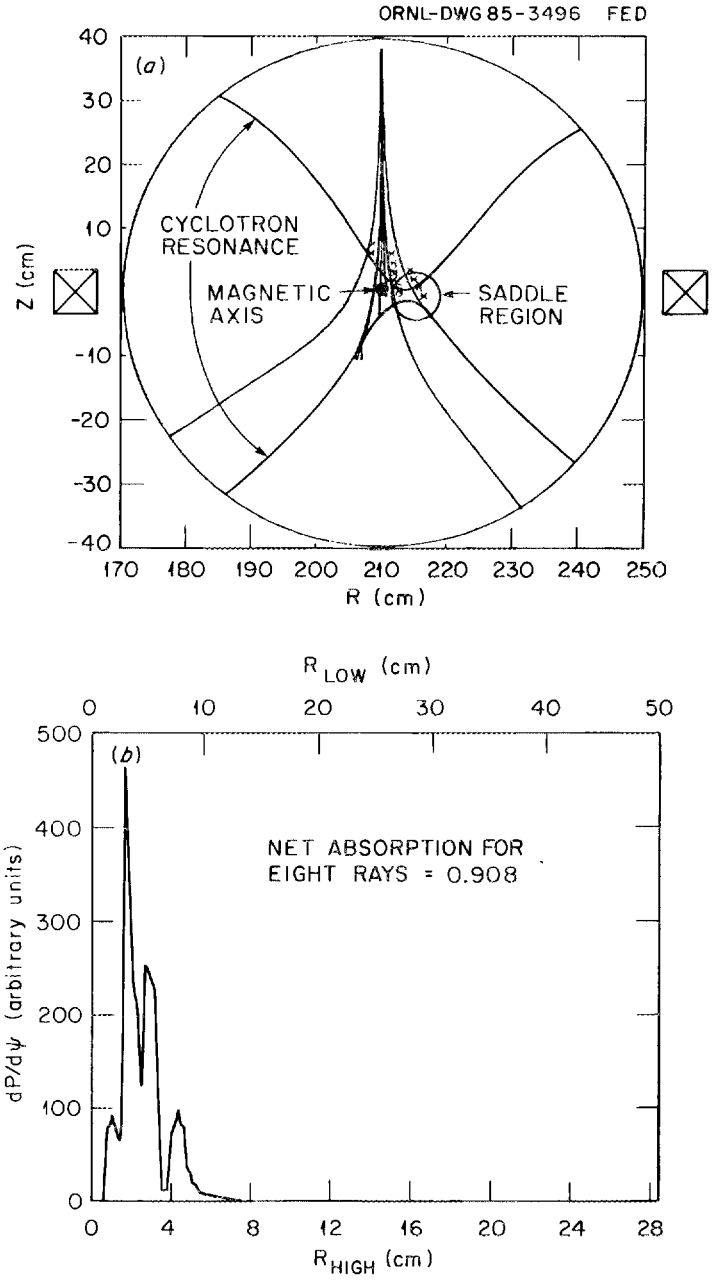

FIG. 18. Low-field $\phi = 0°$ launch. O-mode rays near the fundamental resonance are launched with $n_e = 2.8 \times 10^{13}$ cm^{-3} (O-mode cutoff density $= 3.5 \times 10^{13}$ cm^{-3}).

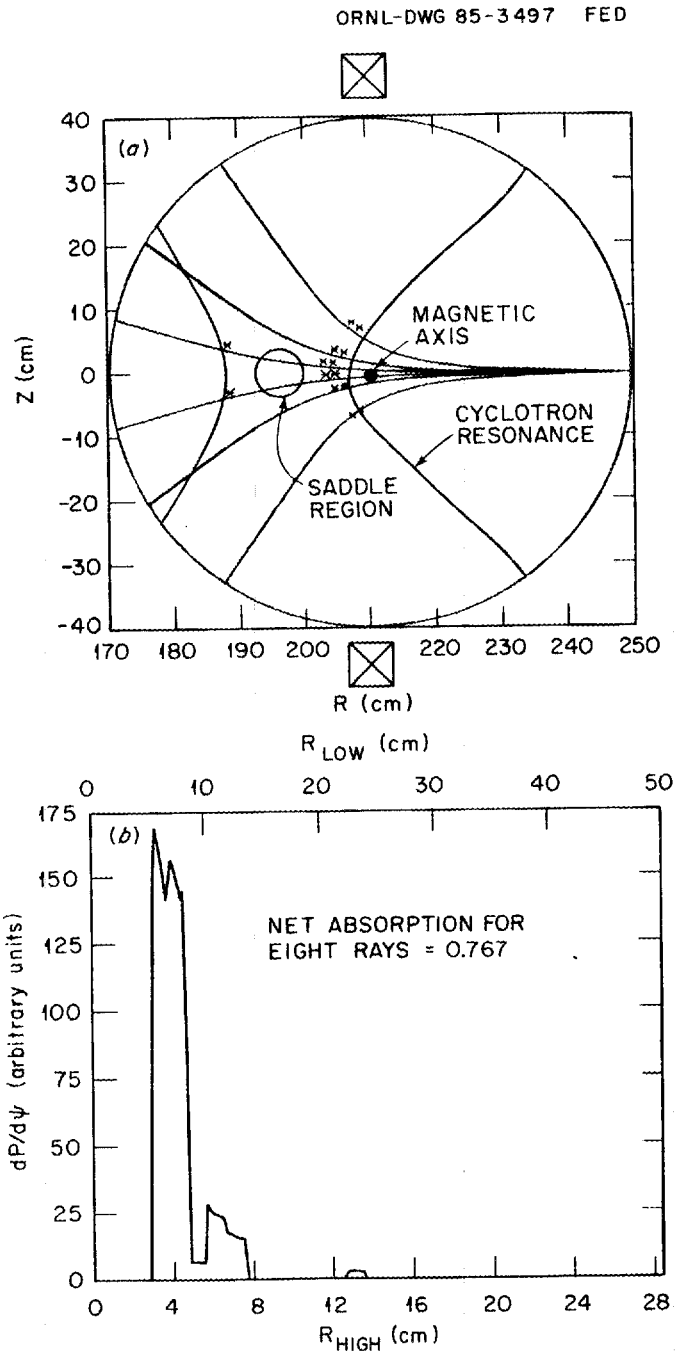

FIG. 19. Low-field $\phi = 15°$ launch. O-mode rays near the fundamental resonance are launched with $n_e = 2.8 \times 10^{13}$ cm^{-3}.

from the $\phi = 0°$ and $\phi = 15°$ toroidal planes, respectively, at a density of 2.8×10^{13} cm^{-3}, which is 80% of the O-mode cutoff. Comparison with point "F" in Figs. 11b and 13b, respectively, reveals that there is little difference in the total absorption or the profiles. The main difference is a scattering of the rays away from the center as it approaches cutoff. If the density were increased any further to make the center inaccessible, then the rays would miss the resonance and the first-pass absorption would drop to zero. Figures 20 and 21 show the high-density cases ($n_e = 1.7 \times 10^{13}$ cm^{-3}) for second harmonic operation and are to be compared with point "B" in Figs. 11 and 13. Again we see that the absorption is similar for densities approaching cutoff. These calculations thus indicate that first-pass heating should continue very close to cutoff and thereafter suddenly vanish.

3.6. WIDE BEAM, DISPLACED AXIS CALCULATIONS

In this section we briefly summarize (without presenting figures) calculations that were done to qualitatively test sensitivity to antenna characteristics and the effect of a displaced magnetic axis. The wide beam case was simulated by launching eight rays in a pattern with a full width at half maximum of 10°. The other first-pass runs described in this paper used a width of 3°. For the displaced axis runs we moved the axis 2 cm radially inward with respect to the beam. The displaced axis runs test the effect on heating if the magnetic axis is not at the nominal radius of 210 cm due to finite beta effects or if VF coil currents are different from those intended. These runs also test the effect of unanticipated asymmetry, such as profile effects or the antenna beam axis not being directly aimed at the magnetic axis. The displaced axis runs were done only at $\phi = 0°$ with low-field launch, which implies that the magnetic axis has moved normal to the beam axis. We did not do $\phi = 15°$ low-field launch with the displaced axis, since in this case the displacement is along the beam and is therefore presumed to have slight effect.

Basically we find that these two effects reduce the total absorption somewhat (or move its location farther out), but not disastrously. For low-field launch fundamental operation at $\phi = 0°$, approximately 90% absorption is still possible, although the radius at which this heating takes place has moved outward from the magnetic axis by 1 or 2 cm. The "detuning" effect is similar for either wide beams or displaced axis. At $\phi = 15°$, recall that the fundamental mode has strong absorption only when the resonance is positioned to cause heating at ~10 cm. The effect of either wide beam or displaced axis is to reduce the heating to 70–80% at about the same radius. For second harmonic, the effects are similar at $\phi = 0°$; 100% absorption is still possible, but it occurs 1–3 cm farther out. At $\phi = 15°$,

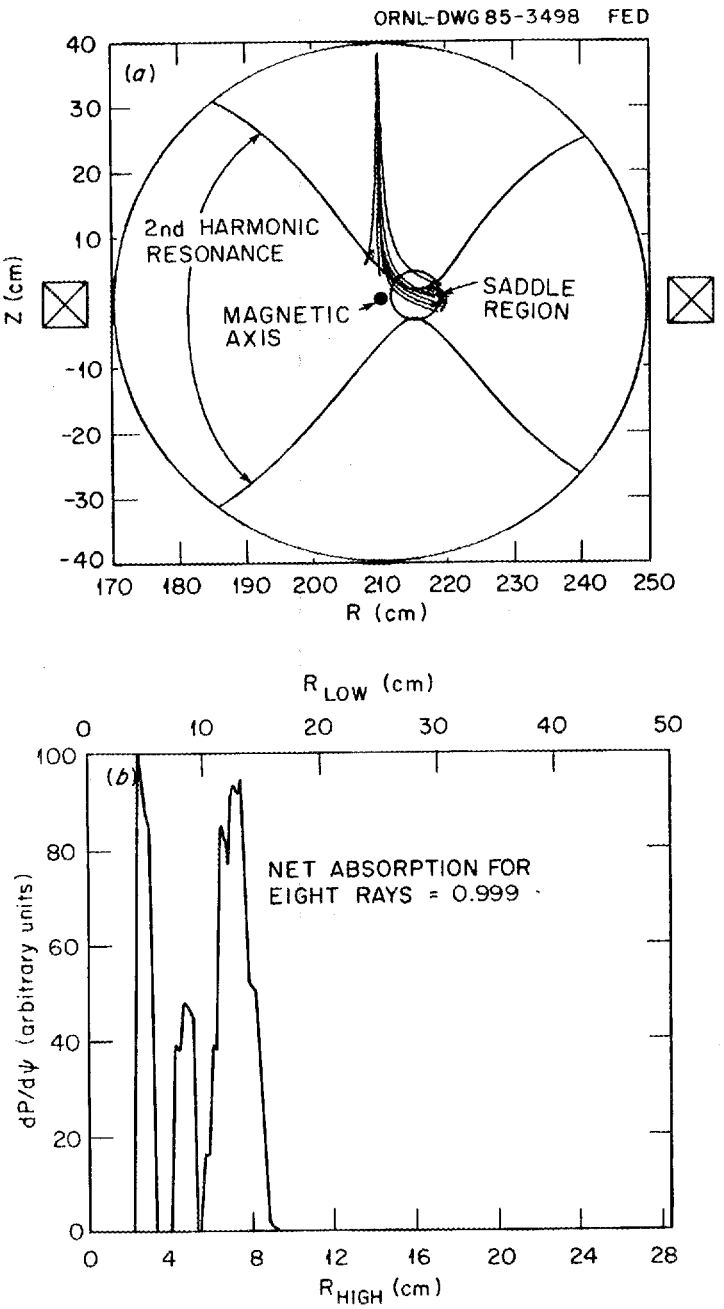

FIG. 20. Low-field $\phi = 0°$ launch. X-mode rays near the second harmonic resonance are launched with $n_e = 1.7 \times 10^{13}$ cm^{-3} (X-mode cutoff density $= 1.8 \times 10^{13}$ cm^{-3}).

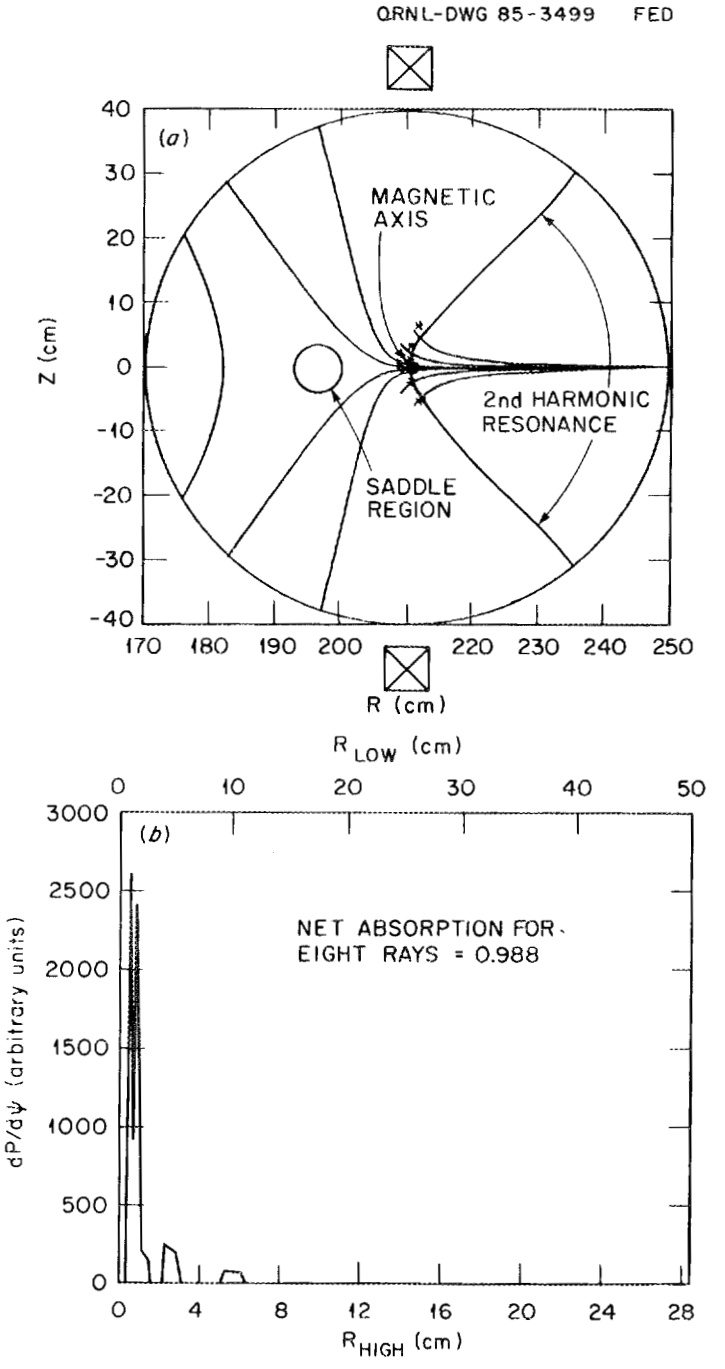

FIG. 21. Low-field $\phi = 15°$ launch. X-mode rays near the second harmonic resonance are launched with $n_e = 1.7 \times 10^{13}$ cm^{-3}.

recall that the second harmonic is 100% absorbed within 2 or 3 cm of the axis. The effect of the wide beam or displaced axis is to move this heating only 1 or 2 cm out.

In summary, these "detuning effects" cause slight degradation in the heating, but the basic conclusions that were reached still stand.

3.7. WALL REFLECTION CALCULATIONS

The wall reflection calculations predict the fate of the power that is not absorbed on the beam's first pass through the plasma. For an idealized launcher, as modeled by the first-pass calculations, the power will reach the plasma center as pure O- or X-mode for operation at the first or second harmonic, respectively. Trade-offs in antenna design for polarization control versus directivity, as well as shear of the magnetic field (which couples O- and X-modes in the beam as it traverses the low-density region of the the plasma), result in a superposition of modes being launched into the plasma. The power that is not absorbed on the first pass will strike a wall and be reflected at the stainless steel wall. To satisfy Maxwell's equations, the reflected wave will consist of a superposition of both O- and X-mode rays. Similar calculations for the EBT device [14,15] showed that there is approximately an equal partition into the two modes and that the highly conductive walls absorb less than 0.5% of the power per bounce. After a few bounces, the non-absorbed power will be scattered throughout the machine as nearly equal amounts of O- and X-mode and will ultimately be absorbed somewhere in the plasma. It is the goal of these wall reflection calculations to estimate where the power is absorbed.

To model this complex problem, we trace a large number of rays (usually 96) for a given mode (O or X) and magnetic field level. These rays are traced for one pass from several representative launch points and numerous launch angles to give the absorption per bounce for the reflected power. We weight the relative importance of each of these discrete rays so as to simulate a uniform and continuous distribution of power going into all directions. Thus the approximation used is that after a few bounces, the vacuum chamber is a homogeneous, isotropic radiator of the remaining power. The weight assigned to each ray's contribution is determined as follows. We assume that all the power radiated from a launch point on the wall is radiated uniformly into the 2π steradians that make up the forward hemisphere facing the plasma. The initialization of the ray directions is set up in the RAYS code with do-loops incrementing equal intervals in θ and ϕ (the azimuthal and polar angles measured with respect to the forward direction). The forward hemisphere is divided into patches, each of which has a ray piercing the center of it. The power passing through this patch is assumed constant over the patch and represented by the associated ray. Then the weight assigned to each ray is

$$W_{ij} = \frac{\Delta\phi}{\pi} \sin(\theta_i) \sin\left(\frac{\Delta\theta}{2}\right) \tag{11}$$

where the ij indices refer to θ_i, θ_j, and $\Delta\theta, \Delta\phi$ refer to the increments for the respective angles. The normalization used here assumes that 100% of the power is emitted into the hemisphere and that the power density per unit solid angle is constant. If the RAYS code is initialized with θ and ϕ running from 0 to π and 0 to 2π, respectively, then the result of tracing this ensemble of rays will be given by a superposition

$$\begin{aligned} P(\bar{r}) &= \sum W_{ij} f_{ij}(\bar{r}) \\ \theta_i &= 0, \pi \\ \phi_j &= 0, 2\pi \end{aligned} \tag{12}$$

where $f_{ij}(\bar{r})$ refers to the spatial power absorption profile for the (i,j)th ray.

Figures 22 and 23 show the power deposition profiles for rays at the fundamental resonance $[\omega_{ce}(0)/\omega = 1]$ for the O- and X-modes, respectively. In Fig. 22 the O-mode histogram is peaked surprisingly close to the center, with median radius near 6 cm. The absorbed power per bounce of this ensemble of rays is 5.4%. The reason for the central peaking is that the O-mode absorption is comparatively weak (remember that damping is an exponential process so weaker damping produces a sharper central peak), is peaked at perpendicular incidence, and is weighted by density, temperature, scale length, and angle of propagation. Thus rays passing near the center are preferentially absorbed. In contrast, Fig. 23 shows that X-mode absorption occurs throughout the plasma and that the absorption per bounce is 24%. We understand this result since the X-mode absorption becomes stronger as the angle with the field decreases. Thus those rays propagating near the center undergo weak absorption due to their nearly perpendicular incidence. The total picture that emerges for steady-state fundamental heating is the following. The beam is launched, reaching the center as nearly pure O-mode (under optimum conditions). The fraction of power not absorbed near the center quickly becomes scrambled in space and polarization. This remaining power will be absorbed mostly in the X-mode and will do little to improve plasma parameters since the deposition is far off-axis. Therefore, it is important to optimize the O-mode first-pass absorption through control of polarization, beam characteristics, and frequency.

Figure 24 shows the power deposition profile for an ensemble of X-mode rays at the second harmonic $[\omega_{ce}(0)/\omega = 0.5]$. The O-mode component has practically no second harmonic absorption, and all the residual power is absorbed from the X-mode. The power is mostly absorbed within 15 cm in the low-field direction, with absorption of about 8%

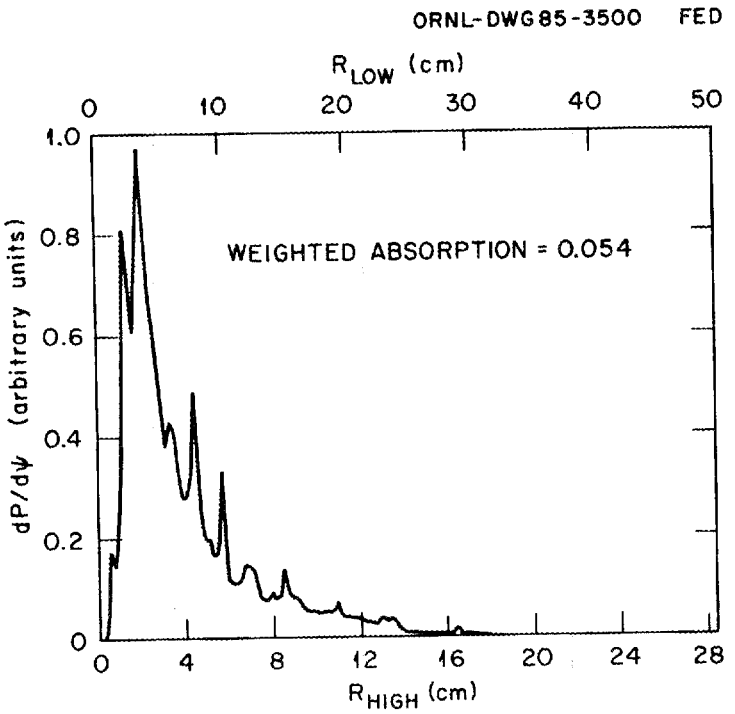

FIG. 22. Power deposition profile for O-mode rays using the wall reflection model. The magnetic axis lies on the fundamental resonance.

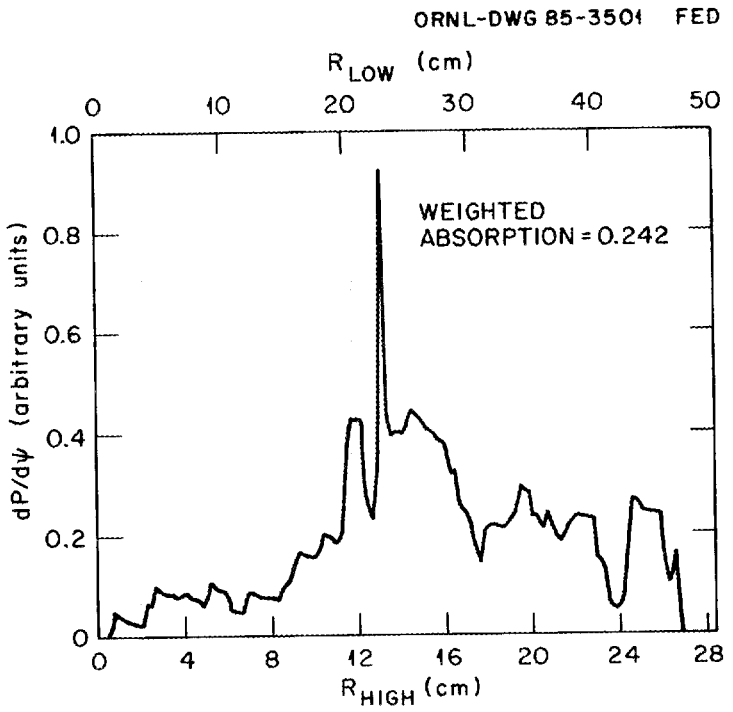

FIG. 23. Power deposition profile for X-mode rays using the wall reflection model. The magnetic axis lies on the fundamental resonance.

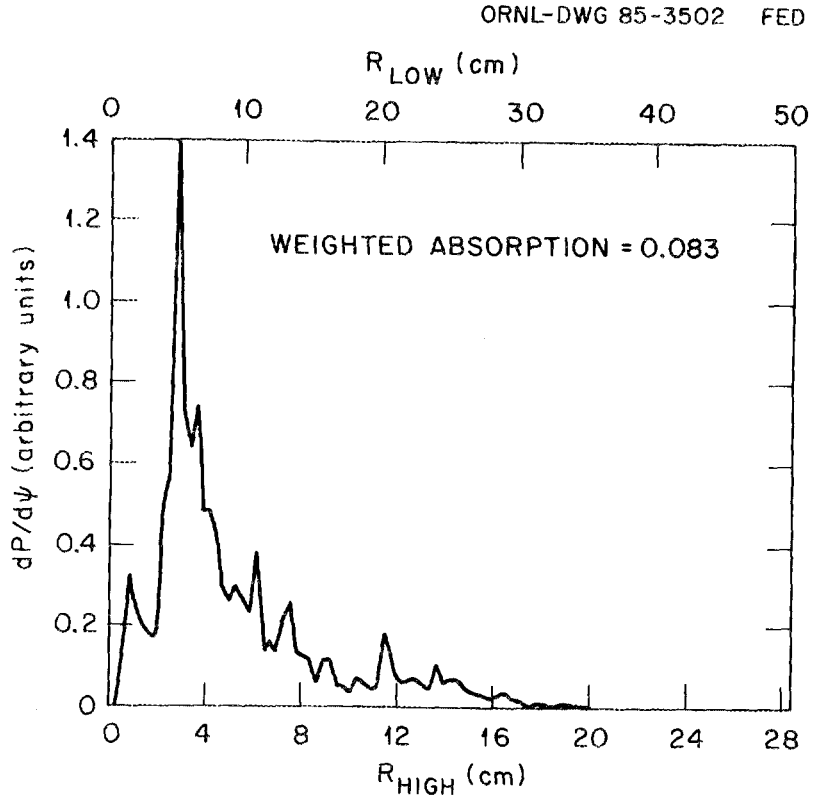

FIG. 24. Power deposition profile for X-mode rays using the wall reflection model. The magnetic axis lies on the second harmonic resonance.

per bounce. These calculations suggest that the wall reflections will make a contribution to useful heat deposited in the plasma for second harmonic operation. Therefore, antenna design (aiming, collimation) and polarization control do not seem as crucial at the second harmonic as they do at the first.

4. SUMMARY AND CONCLUSIONS

Calculations have been done to predict the effects of electron cyclotron heating for the steady-state parameters anticipated in the ATF experiment under construction at ORNL. We have used geometrical optics to study wave propagation and absorption near the fundamental and second electron cyclotron harmonics. The effect of the first pass of the simulated beam has been studied, as has the result of the residual power reflected from the walls.

We find that with control of antenna characteristics (aiming, collimation, polarization) and magnetic field level, it is possible to achieve significant wave absorption near the magnetic axis. Through control of the magnetic field intensity, the first or second harmonic resonance of the wave frequency can be made to fall directly on the magnetic axis. However, the first-pass absorption in this case is generally less than 100%. The topology of the magnetic field is quite complicated with significant toroidal effects. When the resonance is placed on the saddle point in the field (in contrast to having the axis resonant), the absorption becomes total for both first and second harmonic operation. Thus, adjustment of the field level with respect to the wave frequency is a compromise, in most cases, between maximizing the first-pass absorption (saddle point resonant) and depositing the power directly on axis (axis region resonant).

Due to toroidal effects, the topology of the magnetic field is quite different in different toroidal planes. For example, low-field launch in the $\phi = 0°$ plane (from the top) produces results different from those of low-field launch on the $\phi = 15°$ plane. In the $\phi = 0°$ plane the field level at the saddle point is 99.5% of the field at the axis, which is 4 cm inside the saddle point. At $\phi = 15°$, on the other hand, the field at the saddle point is 104.5% of the field at the axis, and the saddle point is about 14 cm inside the axis. Thus, adjustment of the field level and aiming of the beam are quite different for the two launch planes. There are theoretical advantages to launching the beam in the midplane (i.e., horizontally) because of up/down symmetry. This implies low-field launch for $\phi = 15°$ and high-field launch for $\phi = 0°$. With horizontal launch, the beam can simply be aimed perpendicular to the wall towards the plasma, and symmetry will ensure that the beam passes through both the saddle point and the axis. Furthermore, as operating conditons change (e.g., vertical field currents, finite beta effects), these points will remain in the beam path as they move radially in or out. For top launch the geometry is very different: the saddle point and axis are not colinear along the beam, and radial motion of these points is transverse to the beam.

Ordinary mode polarization is desired when the axis is resonant near the fundamental, and X-mode is desired for second harmonic operation. With the steady-state parameters

assumed here ($n_e = 10^{13}$ cm^{-3}, $T_e = 500$ eV), the damping rate at the second harmonic is about five times greater than the rate at the fundamental. This produces slightly different conclusions for the two modes of operation. Because the magnetic scale length near the axis is shorter at $\phi = 15°$ than at $\phi = 0°$, the damping rate is less, and it is not possible to get 100% on-axis absorption for the fundamental mode in the $\phi = 15°$ plane. Thus, low-field launch works slightly better in the $\phi = 0°$ plane than it does for $\phi = 15°$ at the fundamental resonance. When the field is decreased to make the center resonant at the second harmonic in the $\phi = 15°$ plane, the increased damping means that it is possible to have 100% absorption very near the axis. For second harmonic operation, we conclude that the $\phi = 15°$ toroidal plane is superior. We also did runs for higher density and found that the heating continues efficiently as the density is increased towards the cutoff values for both fundamental and second harmonic operation. As the density approaches cutoff, ray refraction increases away from the center until the heating abruptly vanishes at cutoff. Briefly mentioned were the effects of a wider beam and a magnetic axis radially shifted from its nominal location at $R = 210$ cm. These effects give a rough idea of sensitivity to beam aiming, collimation problems, finite beta effects (which radially shift the magnetic axis), and related geometric effects. We found that the heating was degraded slightly (due to either lower total absorption or an outward shift of the heating by several centimeters), but that the basic results and conclusions remained the same.

The effect of wall reflections, due to the non-absorbed portion of the beam, turns out to be an important question beyond the obvious case of a plasma that absorbs less than 100% of the incident beam. Finite beam width, aiming problems, and changing operating conditions all imply that significant power can remain after the first pass. Another problem is due to lack of polarization control. The complex, sheared magnetic field in ATF means that it is difficult to construct an antenna that will place the desired mode in the center. Therefore, the actual radiation at the center will be a superposition of O- and X-modes. A complicated calculation was done in which the vacuum chamber walls were assumed to be an isotropic, homogeneous radiator of power back into the plasma. We find that for operation at the fundamental resonance, the X-mode will be absorbed heavily throughout the plasma (except near the center). The O-mode, fundamental, residual power will be preferentially absorbed at the center but at a rate one-quarter that of the X-mode. This leads us to conclude that the X-mode will dominate and that the residual power will be absorbed on outer flux surfaces. It is important, therefore, to maximize the first-pass fundamental absorption and not rely on reflected power. For second harmonic operation, only the X-mode makes a significant contribution, due to weak absorption of the O-mode. We find that the reflected power for the second harmonic X-mode actually does contribute

to useful heating, with the majority of residual power absorbed within 15 cm of the axis. Second harmonic operation may allow more leeway, or design flexibility, in antenna designs. For startup operation, the absorption rate becomes vanishingly small, and it is crucial that the resonance be placed at the saddle point in the field. This means that antenna design may not be critical for startup, although control of the magnetic field level is vital.

In summary, electron cyclotron heating should be an effective source of central heating in the steady-state ATF plasma. The absorption process is a strong one, and in these idealized calculations, it is possible to place 100% of the power very near the magnetic axis for both first and second harmonic operation. The complicated, three-dimensional magnetic field in this torsatron geometry profoundly affects the results. Only detailed calculations such as these can predict the outcome of a given heating experiment.

REFERENCES

1. BATCHELOR, D. B., GOLDFINGER, R. C., RAYS: A Geometrical Optics Code for EBT, Oak Ridge National Laboratory Rep. ORNL/TM-6844 (1982).
2. BATCHELOR, D. B., GOLDFINGER, R. C., WEITZNER, H., IEEE Trans. Plasma Sci. PS-8 (1980) 78.
3. BATCHELOR, D. B., GOLDFINGER, R. C., Nucl. Fusion 20 (1980) 403.
4. WEITZNER, H., BATCHELOR, D. B., Phys. Fluids 23 (1980) 1359.
5. STIX, T. H., Phys. Rev. Lett. 15 (1965) 878.
6. WHITE, R. B., CHEN, F. F., Plasma Phys. 16 (1974) 565.
7. SCHUSS, J. J., HOSEA, J. C., Phys. Fluids 18 (1975) 727.
8. AKHIEZER, A. I., AKHIEZER, I. A., POLOVIN, R. B., SITENKO, A. G., STEPANOV, K. N., Plasma Electrodynamics, Vol. I, Pergamon Press, Oxford (1975).
9. SHKAROFSKY, I. P., Phys. Fluids 9 (1966) 561, 570.
10. BATCHELOR, D. B., GOLDFINGER, R. C., WEITZNER, H., Phys. Fluids 27 (1984) 2835.
11. CARRERAS, B. A., HICKS, H. R., HOLMES, J. A., LYNCH, V. E., GARCIA, L., et al., Phys. Fluids 26 (1983) 3579.
12. LYON, J. F., CARRERAS, B. A., HARRIS, J. H., ROME, J. A., DORY, R. A., et al., Stellarator Physics Evaluation Studies, Oak Ridge National Laboratory Rep. ORNL/TM-8496 (1983).
13. LYNCH, V. E., CARRERAS, B. A., CHARLTON, L. A., HENDER, T. C., GARCIA, L., et al., Oak Ridge National Laboratory Rep. ORNL/TM-9861 (to be published).
14. WHITE, T. L., Oak Ridge National Laboratory, private communication, 1985.
15. BATCHELOR, D. B., GOLDFINGER, R. C., RASMUSSEN, D. A., Phys. Fluids 27 (1984) 948.

ORNL/TM-9869
Dist. Category UC-20g

INTERNAL DISTRIBUTION

1-5. D. B. Batchelor
6. T. S. Bigelow
7. J. L. Cantrell
8. B. A. Carreras
9. W. A. Cooper
10. R. A. Dory
11. R. H. Fowler
12. L. Garcia
13. J. C. Glowienka
14-18. R. C. Goldfinger
19. J. H. Harris
20. J. A. Holmes
21. W. A. Houlberg
22. H. C. Howe
23. D. K. Lee
24. V. E. Lynch
25. J. F. Lyon
26. L. W. Owen
27. J. A. Rome
28. D. A. Spong
29. T. L. White
30. J. Sheffield
31-32. Laboratory Records Department
33. Laboratory Records, ORNL-RC
34. Document Reference Section
35. Central Research Library
36. Fusion Energy Division Library
37-38. Fusion Energy Division Publications Office
39. ORNL Patent Office

EXTERNAL DISTRIBUTION

40. Office of the Assistant Manager for Energy Research and Development, Department of Energy, Oak Ridge Operations Office, P. O. Box E, Oak Ridge, TN 37831
41. J. D. Callen, Department of Nuclear Engineering, University of Wisconsin, Madison, WI 53706
42. J. F. Clarke, Office of Fusion Energy, Office of Energy Research, ER-50, Germantown, U.S. Department of Energy, Washington, DC 20545
43. R. W. Conn, Department of Chemical, Nuclear, and Thermal Engineering, University of California, Los Angeles, CA 90024

44. S. O. Dean, Director, Fusion Energy Development, Science Applications International Corporation, Gaithersburg, MD 20879
45. H. K. Forsen, Bechtel Group, Inc., Research Engineering, P. O. Box 3965, San Francisco, CA 94105
46. J. R. Gilleland, GA Technologies, Inc., Fusion and Advanced Technology, P.O. Box 81608, San Diego, CA 92138
47. R. W. Gould, Department of Applied Physics, California Institute of Technology, Pasadena, CA 91125
48. R. A. Gross, Plasma Research Library, Columbia University, New York, NY 10027
49. D. M. Meade, Princeton Plasma Physics Laboratory, P.O. Box 451, Princeton, NJ 08544
50. M. Roberts, International Programs, Office of Fusion Energy, Office of Energy Research, ER-52, U.S. Department of Energy, Washington, DC 20545
51. W. M. Stacey, School of Nuclear Engineering and Health Physics, Georgia Institute of Technology, Atlanta, GA 30332
52. D. Steiner, Nuclear Engineering Department, NES Building, Tibbetts Avenue, Rensselaer Polytechnic Institute, Troy, NY 12181
53. R. Varma, Physical Research Laboratory, Navrangpura, Ahmedabad 380009, India
54. Bibliothek, Max-Planck Institut fur Plasmaphysik, D-8046 Garching, Federal Republic of Germany
55. Bibliothek, Institut fur Plasmaphysik, KFA, Postfach 1913, D-5170 Julich, Federal Republic of Germany
56. Bibliotheque, Centre des Recherches en Physique des Plasmas, 21 Avenue des Bains, 1007 Lausanne, Switzerland
57. Bibliotheque, Service du Confinement des Plasmas, CEN/Cadarache, Departement de Recherches sur la Fusion Controlee, 13108 Saint-Paul-lez-Durance, France
58. Documentation S.I.G.N., Departement de la Physique du Plasma et de la Fusion Controlee, Centre d'Etudes Nucleaires, B.P. 85, Centre du Tri, 38041 Grenoble, France
59. Library, Culham Laboratory, UKAEA, Abingdon, Oxfordshire, OX14 3DB, England

60. Library, FOM-Instituut voor Plasma-Fysica, Rijnhuizen, Edisonbaan 14, 3439 MN Nieuwegein, The Netherlands
61. Library, Institute of Plasma Physics, Nagoya University, Nagoya 464, Japan
62. Library, International Centre for Theoretical Physics, Trieste, Italy
63. Library, Laboratorio Gas Ionizatti, CP 56, I-00044 Frascati, Rome, Italy
64. Library, Plasma Physics Laboratory, Kyoto University, Gokasho, Uji, Kyoto, Japan
65. Plasma Research Laboratory, Australian National University, P.O. Box 4, Canberra, A.C.T. 2000, Australia
66. Thermonuclear Library, Japan Atomic Energy Research Institute, Tokai-mura, Ibaraki Prefecture, Japan
67. G. A. Eliseev, I. V. Kurchatov Institute of Atomic Energy, P. O. Box 3402, 123182 Moscow, U.S.S.R.
68. V. A. Glukhikh, Scientific-Research Institute of Electro-Physical Apparatus, 188631 Leningrad, U.S.S.R.
69. I. Shpigel, Institute of General Physics, U.S.S.R. Academy of Sciences, Ulitsa Vavilova 38, Moscow, U.S.S.R.
70. D. D. Ryutov, Institute of Nuclear Physics, Siberian Branch of the Academy of Sciences of the U.S.S.R., Sovetskaya St. 5, 630090 Novosibirsk, U.S.S.R.
71. V. T. Tolok, Kharkov Physical-Technical Institute, Academical St. 1, 310108 Kharkov, U.S.S.R.
72. Library, Academia Sinica, P.O. Box 3908, Beijing, China (PRC)
73. N. A. Davies, Office of the Associate Director, Office of Fusion Energy, Office of Energy Research, ER-51, Germantown, U.S. Department of Energy, Washington, DC 20545
74. D. B. Nelson, Director, Division of Applied Plasma Physics, Office of Fusion Energy, Office of Energy Research, ER-54, Germantown, U.S. Department of Energy, Washington, DC 20545
75. E. Oktay, Division of Confinement Systems, Office of Fusion Energy, Office of Energy Research, ER-55, Germantown, U.S. Department of Energy, Washington, DC 20545

76. A. L. Opdenaker, Fusion Systems Design Branch, Division of Development and Technology, Office of Fusion Energy, Office of Energy Research, ER-532, Germantown, U.S. Department of Energy, Washington, DC 20545
77. W. Sadowski, Fusion Theory and Computer Services Branch, Division of Applied Plasma Physics, Office of Fusion Energy, Office of Energy Research, ER-541, Germantown, U.S. Department of Energy, Washington, DC 20545
78. P. M. Stone, Fusion Systems Design Branch, Division of Development and Technology, Office of Fusion Energy, Office of Energy Research, ER-532, Germantown, U.S. Department of Energy, Washington, DC 20545
79. J. M. Turner, International Programs, Office of Fusion Energy, Office of Energy Research, ER-52, Germantown, U.S. Department of Energy, Washington, DC 20545
80. R. E. Mickens, Atlanta University, Department of Physics, Atlanta, GA 30314
81. M. N. Rosenbluth, RLM 11.218, Institute for Fusion Studies, University of Texas, Austin, TX 78712
82. Theory Department Read File, c/o D. W. Ross, University of Texas, Institute for Fusion Studies, Austin, TX 78712
83. Theory Department Read File, c/o R. C. Davidson, Director, Plasma Fusion Center, NW 16-202, Massachusetts Institute of Technology, Cambridge, MA 02139
84. Theory Department Read File, c/o F. W. Perkins, Princeton Plasma Physics Laboratory, P.O. Box 451, Princeton, NJ 08544
85. Theory Department Read File, c/o L. Kovrizhnykh, Lebedev Institute of Physics, Academy of Sciences, 53 Leninsky Prospect, 117924 Moscow, U.S.S.R.
86. Theory Department Read File, c/o B. B. Kadomtsev, I. V. Kurchatov Institute of Atomic Energy, P.O. Box 3402, 123182 Moscow, U.S.S.R.
87. Theory Department Read File, c/o T. Kamimura, Institute of Plasma Physics, Nagoya University, Nagoya 464, Japan

88. Theory Department Read File, c/o C. Mercier, Departemente de Recherches sur la Fusion Controlee, B.P. No. 6, F-92260 Fontenay-aux-Roses (Seine), France
89. Theory Department Read File, c/o T. E. Stringer, JET Joint Undertaking, Culham Laboratory, Abingdon, Oxfordshire OX14 3DB, England
90. Theory Department Read File, c/o K. Roberts, Culham Laboratory, Abingdon, Oxfordshire OX14 3DB, England
91. Theory Department Read File, c/o D. Biskamp, Max-Planck-Institut fur Plasmaphysik, D-8046 Garching, Federal Republic of Germany
92. Theory Department Read File, c/o T. Takeda, Japan Atomic Energy Research Institute, Tokai-mura, Ibaraki Prefecture, Japan
93. Theory Department Read File, c/o C. S. Liu, GA Technologies, Inc., P.O. Box 81608, San Diego, CA 92138
94. Theory Department Read File, c/o L. D. Pearlstein, L-630, Lawrence Livermore National Laboratory, P.O. Box 5511, Livermore, CA 94550
95. Theory Department Read File, c/o R. Gerwin, CTR Division, Los Alamos National Laboratory, P.O. Box 1663, Los Alamos, NM 87545

96-247. Given distribution according to TIC-4500, Magnetic Fusion Energy (Distribution Category UC-20g, Theoretical Plasma Physics)